Recent developments in magnetic nanostructures

J. L. Morán-López[1,7,*], R. A. Guirado-López[2], J. M. Montejano-Carrizalez[2], F. Aguilera-Granja[2], R. Rodríguez-Alba[3], José Mejía-López[4], Aldo H. Romero[5] and Martin E. Garcia[6]

[1]Center for Computational Materials, Institute for Computacional Engineering and Sciences, University of Texas at Austin, Austin, TX 78712-0027, USA
[2]Instituto de Física 'Manuel Sandoval Vallarta', and [3]Department of Physics and Mathematics, Universidad Autónoma de San Luis Potosí, Alvaro Obregón 64, 78000 San Luis Potosí, México
[4]Pontificia Universidad Católica de Chile, Facultad de Física, casilla 306, Santiago 22, Chile
[5]CINVESTAV Querétaro, Libramiento Norponiente No. 2000, 76230 Querétaro, Mexico
[6]Theoretische Physik, Fachbereich Naturwissenschaften, and Center for Interdisciplinary Nanostructure Science and Technology (CINSaT), Universität Kassel, Heinrich-Plett-Str. 40, 34132 Kassel, Germany
[7]Present address: Universidad Politécnica de San Luis Potosí

Some of the new developments on magnetic nanostructures are reviewed. The advances on the synthesis, characterization, and understanding of magnetic dimers, nanoclusters, magnetic nanowires, Heusler alloy thin films, and single molecule magnets, are discussed. Particular emphasis is made on the magnetic properties of: (a) manganese dimer, whose properties is a field of debate and are important to disentangle the multifarious behaviour of the macroscopic samples, (b) manganese nanostructures which show a very rich and complex behaviour, not shown in other transition metal clusters, (c) cobalt magnetic nanowires, which show spin-reorientations as a function of size and microstructure, (d) Heusler alloys, that are half-metallic present potential applications for spintronics, and magnetic shape memory devices, and (e) single molecule magnets, systems with very high magnetic moments and are homogeneous in macroscopic samples. All these systems are good candidates for technological applications and in particular for the emerging field of spintronics.

Keywords: Cobalt nanostructures, magnetic nanostructures, magnetic nanowires, manganese nanostructures.

Introduction

DUE to the effects of special confinement and low dimensionality, ultra thin films, nanowires, and clusters of atoms composed of transition metal atoms exhibit magnetic properties not displayed by the corresponding bulk solids. For example, elements that do not show magnetic phases in bulk samples, like rhodium, display magnetic moments in small clusters[1]. Furthermore, due to recent advances in experimental techniques, nowadays one can synthesize, characterize and design special materials with specific size, composition and structure. It is interesting that these new materials show unexpected physicochemical properties that are not interpolations between the atomic or molecular structures and the bulk solids. These effects are recognized to be produced mainly by the large ratio between surface and bulk atoms[2].

In particular, the magnetic properties of low dimensional systems are of great importance from both, the point of view of fundamental understanding, for the potential applications in storage media, medical applications and pharmacology. Careful measurements of the magnetic properties of small magnetic aggregates, nanowire arrays, and single molecule magnets have been published in the last decade. In the case of small atomic clusters, most of them show an enhancement in the atomic magnetic moments and a smooth size dependence[3]. An exemption is manganese, which by far is the most complicated magnetic element. The size dependence of the magnetic moment is non-monotonic with various maxima[4,5].

On the other hand, other systems that exhibit potential technological applications are nanowires of magnetic transition metals. Transition metal (TM) nanowires are among the most studied magnetic nanostructures. In particular, a large amount of previous experimental reports have shown that single component as well as alloyed TM nanowire arrays synthesized by electrodeposition into porous membranes can be fabricated (see for example ref. 6) and that they are characterized by having magnetic properties (e.g. hysteresis curves[7–9], Curie temperature[10], magnetization reversal mechanisms[7,11,12], etc.) that strongly depend on relatively easy experimentally accessible parameters like for example, the wires length and diameter, inter-wire coupling, microstructure, and the chemical composition of the samples.

Here, we address a few particular systems. First, we report on recent results on the magnetic properties of

*For correspondence. (e-mail: jlmoran-lopez@upslp.edu.mx)

manganese dimer[13]. It is important to understand this basic unit in order to shed some light on the very complex behaviour of manganese systems. We present next recent results on the size dependence of the magnetic properties of manganese clusters[14]. Then, we mention results on the magnetocrystalline anisotropic energy as well as local spin and orbital magnetic moments for finite length Co nanowires[15]. The recent interest of Heusler alloy films for its half-metallic behaviour as well as memory shape properties is discussed next. Here, we present a simplified two-dimensional model studied recently[16]. Recently, the discovery of complex Mn-molecules that function as nanoscale magnets has been reported[17,18,19]. These intricate molecules with Mn_{12}- and Mn_4-complexes act as single-domain magnetic particles that, below their blocking temperature, exhibit magnetization hysteresis. These systems will be addressed in more detail. Finally, we summarize the issues discussed here.

The manganese dimer

The magnetic properties of manganese have represented a challenge for many decades. Manganese is a unique element which exhibits a variety of unusual crystallographic, electronic, and magnetic properties depending on the pressure, temperature, and its ennvironment[17–24]. We believe that in order to understand that complex behaviour, it is of major relevance to understand the manganese dimer.

To appreciate the complexity of Mn systems let us mention some of the properties of bulk samples, which show many intricate crystallographic structures and multifarious behaviours. The α-Mn at ambient conditions is paramagnetic and its crystal structure cell contains 58 atoms. At temperatures below the Neel temperature $T_N = 95$ K, it adopts a complex noncollinear antiferromagnetic phase. In addition, the magnetic phase transition is coupled to a crystal lattice distortion[25]. Upon increasing the temperature to 1000 K, the solid undergoes a crystallographic transition to a cubic lattice (β-phase) with 20 atoms per unit cell[26]. The γ-phase is observed in the range from 1368 to 1406 K. Finally, from this last temperature to the melting point $T_M = 1517$, manganese adopts the δ-phase, which has a bcc structure.

On the other hand, by quenching the γ-phase to room temperature a face-centered-tetragonal structure is stabilized. This phase is antiferromagnetic with a Neel temperature of $T_N = 570$ K. Furthermore, recent high pressure experiments[27] report a change of phase from the α- to the ε-phase that seems to be an antiferromagnet with bcc structure and Neel temperature of $T_N = 450$ K.

Other interesting characteristic of manganese systems is that dilute solutions of Mn in Cu and Ag behave like spin glasses[20]. These spin glass systems have the properties of a Heisenberg spin system. However, the presence of anisotropies induces an Ising-like state at small magnetic fields. Other intriguing systems with potential technological applications are the manganese oxides known as manganites. They show a colossal magnetoresistance.

Consistently with the remarkable properties of Mn-compounds mentioned above, experiments show that small manganese clusters exhibit a complex magnetic behaviour, with signatures of super paramagnetism and magnetic moments $\mu(n)$ smaller than 1.5 μ_B per atom[4,5,22,23]. The behaviour of systems is discussed in the next section.

Finally, the most simple manganese molecule, the dimer is not fully understood. From the experimental point of view, the bond length obtained by ESR spectroscopy is 3.4 Å, which is very large as compared with the bulk value $d_0 = 2.89$ Å. The measurements were performed by depositing the dimer in rare gas matrices and found that the dimer has a very low dissociation energy $D_0 = 0.1$ eV, and the atomic spins couple antiferromagnetically[23]. A resonance Raman experiment also supports the singlet antiferromagnetic ground state[28] ($^1\Sigma_g^+$). For an extensive review on the experimental research on transition metal and lanthanide small clusters, Lombardi and Davis[24] can be consulted.

It is clear that in an attempt to disentangle the complex behaviour of manganese one must try to understand the properties of the dimer as a basic unit. In recent years, this subject has been a field of intensive theoretical and experimental research but up to now no consensus on its properties has been achieved.

One of the earliest calculations[29] on Mn_2, based on the Hartree–Fock approximation obtained an antiferromagnetic ground state with a bond length of 2.88 Å. More recently, different theoretical determinations of the magnetic and electronic structure of Mn_2 have been reported within the framework of the density functional theory[30–32] and molecular orbit methods[34–36]. The density functional theory calculations yield a ferromagnetic ground-state solution, but the antiferromagnetic solution differs only slightly in energy. Furthermore, a careful analysis within an all-electron scheme came to the conclusion that Mn_2 exhibit multiple magnetic and structural minima[30]. On the other hand, the MO calculations by Wang and Chen[35] and Yamamoto *et al.*[36] yield an antiferromagnetic ground state.

The experimental evidence and the theoretical works mentioned above suggest that the most probable scenario for the magnetic properties of the dimer and small Mn clusters is that of almost degenerate different spin configurations. Therefore, the correct approach to describe their magnetic structure must include non-collinearity. The importance of this property was recognized recently by a calculation which yields a non-collinear magnetic configuration[33] for Mn_6. Moreover, the fact that the ferromagnetic and antiferromagnetic solutions are very close in energy, in particular for very small clusters[31] could also lead to spin frustration in larger clusters. As mentioned above, the overall size dependence of $\mu(n)$ measured by Knickelbein[4,5] was theoretically described recently[14]

on the basis of a non-collinear model for the magnetic moments ground state orientations.

In this section, we present the theoretical description of the dependence of the electronic and magnetic solutions on the interatomic distance for Mn_2. In a very recent paper[14], we find that the magnetic coupling depends very sensitively on the interatomic distance. For short distances the ground state is antiferromagnetic but it changes to ferromagnetic at $d = 3.06$ Å. In particular in our calculation the ground state is antiferromagnetic with an interatomic distance $d = 2.89$ Å.

Calculation

As reported in detail in ref. 14 we performed a non-collinear *ab initio* determination of the magnetic properties of Mn_2. Our results suggest that a remarkable competition between kinetic and exchange-correlation energies leads to almost degenerate spin configurations. To determine the electronic and magnetic properties of the dimer we have used the SIESTA code[37], which performs a fully self-consistent density-functional calculation to solve the Kohn–Sham equations. We included spin polarization, both collinear and noncollinear[38], in the local-density approximation (LDA). The ionic pseudopotentials[39] were generated from the atomic configurations $[Ne]3s^2 3p^6 3d^5 4s^2$. The basis set used to describe the valence states is a double-ζ set with a confining energy shift of 50 meV.

We calculated the solution of the Kohn–Sham equations by fixing the atoms in the dimer at a given distance and by assuming a given magnetic configuration (ferro- and antiferro-magnetic). In addition, we also performed the calculation by permitting that the magnetic moments take any arbitrary direction, i.e. noncollinearity.

Results and discussion

We present in Figure 1 the spin resolved electronic occupation spectra obtained by assuming an antiferromagnetic (AF) arrangement for an interatomic distance $d = 2.6$ Å. Here, we have added a small imaginary part around the energy levels to wide them up and the zero of energy is taken at the highest occupied energy level (HOMO). The contributions coming from the different electronic levels are shown. One notices that the 3s and 3p electronic states are fully occupied since they lie deep in energy and do not contribute to the magnetic moment. The lower part contains a close up to the region around the zero of energy. As shown here, the electrons near the HOMO are the 4s and 3d electrons. The small peaks correspond to the 4s electrons. There is a small number of s states with spin up above the HOMO. As discussed below, these states bring a decrease in the total magnetic moment μ.

In Figure 2, we show the results for the spin resolved electronic occupation spectra assuming the same interatomic distance, but for the ferromagnetic (FM) arrangement. As expected, the role of 3s and 3p electrons is also irrelevant for the magnetic properties of this state of the dimer. In the lower panel we present a close up to the region around the HOMO. In this case the number of spin-up d electrons is 5 and the one of spin-down electrons is zero. In the case of the 4s orbitals, there is one electron with spin-up and other with spin-down.

In Figure 3 we plot how the charge on the 4s and 3d levels change as a function of distance for the antiferromagnetic state. As the distance is decreased, the 3d down-electron state increases its charge at the expenses of the 3d spin-down level. Due to hybridization there is a small charge transfer between s and d states. If the distance is too short the 4s up electrons may be transferred in a larger amount than the spin down. As discussed below, this brings a negative contribution to the total magnetic moment. Let us recall that the results are given per atom and the 3s and 3p electrons are not taken into account in this sum.

The dependence of the occupation of the 4s (upper panel) and 3d (middle panel) levels on the distance be-

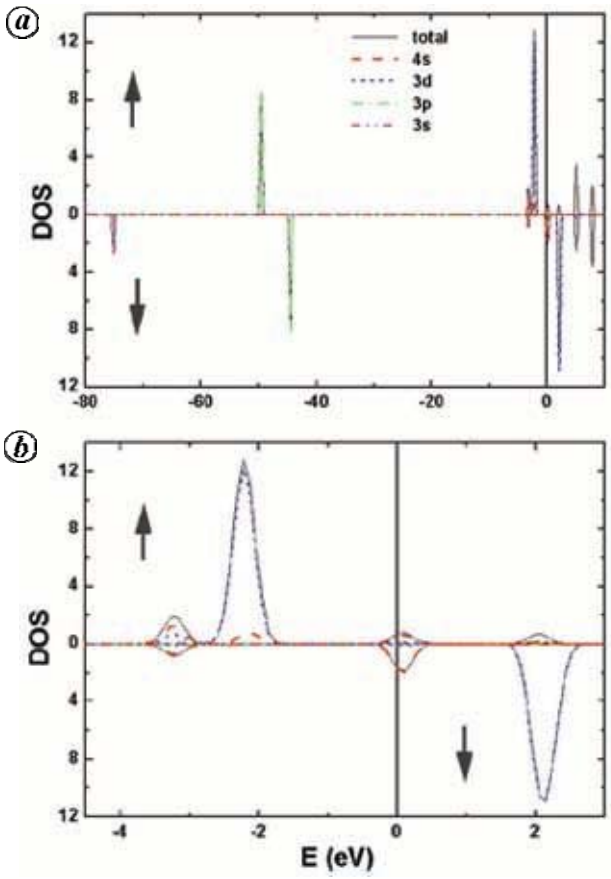

Figure 1. Spin resolved density of states (DOS) of Mn_2 in the antiferromagnetic (AF) state for an interatomic distance of $d = 2.6$ Å. ***a***, Contributions from the s and d orbitals of the whole dimmer. ***b***, Close up of the spin resolved DOS in the AF state for a small energy window around the HOMO.

tween nucleus for the FM alignment is given in Figure 4. The occupation of 3d up-electrons is close to five and the increase in down-electrons as the distance decreases comes more from 4s electrons. It is also to be noticed that there is no crossover behaviour in the distance dependence of the charge of up- and down-electrons. This behaviour brings a positive contribution to the total magnetic moment.

We show in Figure 5 the magnetic moments generated by 4s and 3d electrons. The magnetic moment produced by d electrons is smaller in the AF than the FM case for short distances, and both become equal at a distance of about 3.06 Å. Above that value the FM arrangement has a magnetic moment smaller but very similar value to the AF solution. A more interesting behaviour is observed in the s magnetic moment, which is negative for the AF state at small values of the interatomic distance. In contrast, the magnetic moment of the FM arrangement increases monotonously as the interatomic distance gets shorter. The lower panel contains the distance dependence of the total magnetic moment in the two cases, FM and AF.

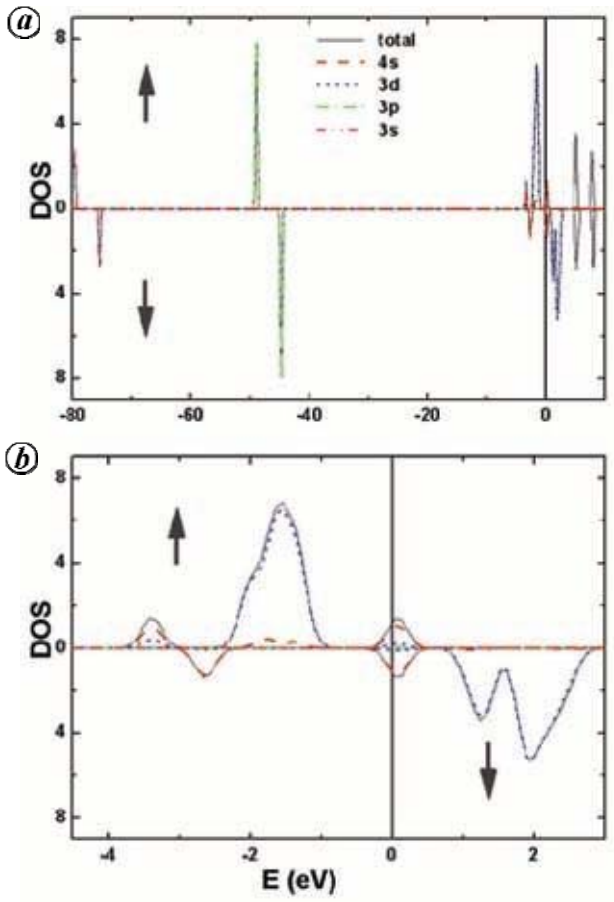

Figure 2. Spin resolved DOS of Mn_2 in the ferromagnetic (FM) state for an interatomic distance of $d = 2.6$ Å. ***a***, Contributions from the s and d orbitals of the whole dimer. ***b***, Close up of the spin resolved DOS in the AF state for a small energy window around the HOMO.

In most of the *ab initio* calculations on Mn clusters reported previously a FM ground state for Mn_2 was obtained. Only as the number of atoms increases a change from FM to AF behaviour was obtained[30–32]. The AF

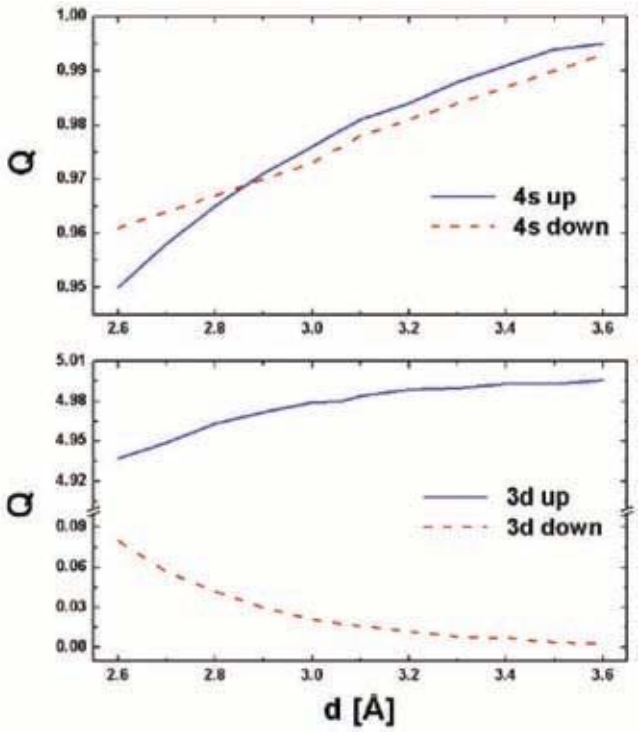

Figure 3. Charge Q of the 4s and 3d orbitals of Mn_2 in the AF state as a function of the interatomic distance.

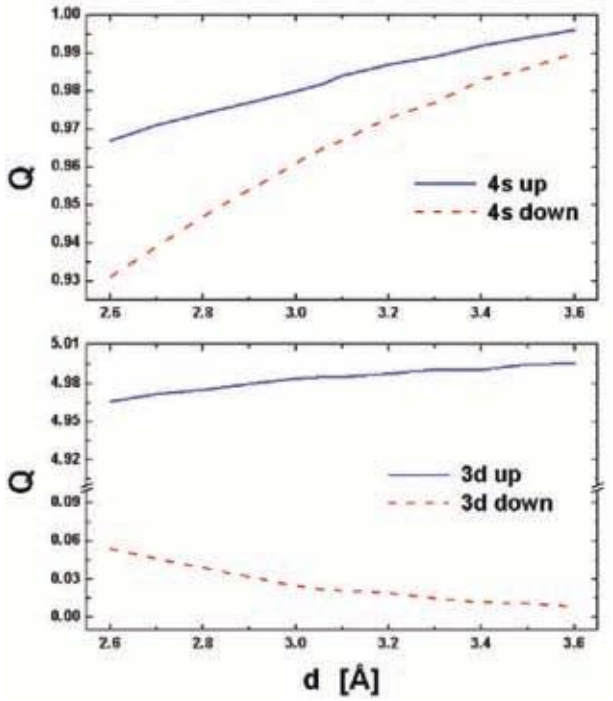

Figure 4. Charge Q of the 4s and 3d orbitals of Mn_2 in the FM state as a function of the interatomic distance.

behaviour was first obtained for clusters with five[31] and nine atoms[30]. Although in a more recent calculation[33] the appearance of noncollinear solutions were obtained for Mn_6.

In contrast, our calculations yield an AF ground state, with a bond length of $d_0 = 2.890$ Å. This result for the magnetic ordering of the dimer is in agreement with the experimental evidences mentioned above[23,24].

However, it must be pointed out that the FM, AF and noncollinear states are almost degenerate. We show in Figure 6 the distance dependence of the total energy for the FM, AF y NC solutions. There is a remarkable distance dependence exhibited by the magnetic coupling, going from AF to a noncollinear (NC) arrangement to FM as the interatomic distance increases.

The most important feature of Figure 6 is that there is a crossing between the FM and AF curves at $d_c = 3.06$ Å, which determines the interatomic distance at which the ground-state changes from AF to FM.

It is important to note that the energy of the noncollinear solution coincides with the AF curve for distances $d < d_c$ and with the FM curve for $d > d_c$. This means that the dimer shows collinear magnetism for almost all distances. However, we obtain an interesting behaviour around $d = d_c$, where the noncollinear solution has a slightly lower energy than the collinear curves. This is due to the fact that at this point the AF and FM states have the same energy and therefore an intermediate noncollinear state leads to an energy decrease.

Another important feature shown by Figure 6 is the appearance of multiple minima in the three energy curves. This is produced by the competition of the various interactions. The different energy terms (exchange, correlation, kinetic energy, Hartree energy and core–core repulsion) compensate each other in such a way that small variations in magnitude of these terms lead to shifts, amplification or disappearance of some of the minima.

Note that the depths of all energy minima of Figure 6 are larger than the error $\Delta\varepsilon$ of the energy calculations, $\Delta\varepsilon < 1$ meV, whereas the heights of the energy barriers are at least 5 meV. It is possible that inclusion of van der Waals interactions (which are not taken into account by the LDA) might lead different and more pronounced minimum.

We have analysed the distance dependence of the different terms contributing to the cohesive energy of the dimer. It turns out that most of the energy terms cancel each other, except the correlation energy, which plays then the fundamental role.

Since the FM and the AF configurations of the dimer are very close in energy, and due to the change of magnetic character for increasing distances, one should not expect a clear magnetic ordering in small clusters, but rather a competition between both types in larger clusters where manganese atoms may be located at distances that favour FM or AF coupling. The fact that nearest neighbours will tend to order antiferromagnetically, whereas further neighbours will favour a ferromagnetic ordering, leads to noncollinear effects and domain formation, in order to avoid spin frustration as much as possible.

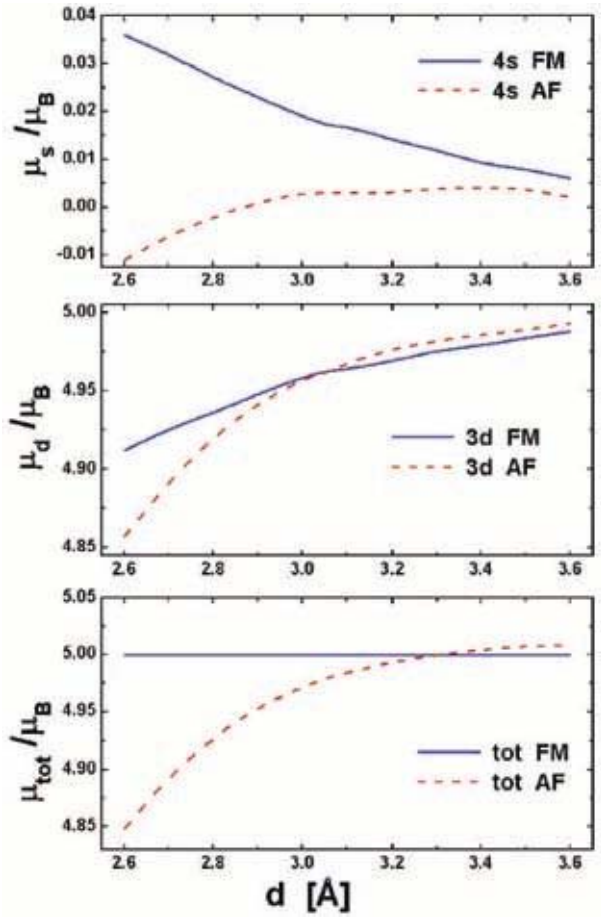

Figure 5. Magnetic moment for each of the atoms of Mn_2 as a function of dimer distance.

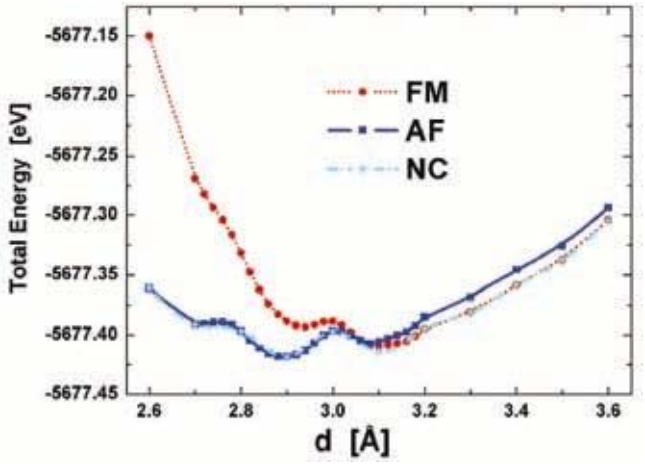

Figure 6. Total energy for Mn_2 as a function of dimer distance.

The behaviour shown in Figure 6 can be interpreted as follows. For short interatomic distances the strong overlap of 3d-orbitals and hybridization effects with 4s electrons lead to electron delocalization, which favours antiferromagnetism. In contrast, for long distances, localization becomes more important and the low hybridization with 4s states lead to a ferromagnetic ground state.

One can analyse the crossing of energy curves within the framework of magnetic coupling constants. We have determined an effective exchange coupling constant $J(d)$ between localized spins at the Mn atoms as defined by

$$J(d) = (E(d)^{\uparrow\downarrow} - E(d)^{\uparrow\uparrow})/2. \quad (1)$$

as a function of the interatomic distance d. This behaviour is shown in Figure 7. As expected, we obtain $J > 0$ for $d < d_c$ (antiferromagnetic coupling) and $J < 0$ for $d > d_c$ (ferromagnetic coupling).

Conclusions

A theoretical description of the dependence of the electronic and magnetic solution on the interatomic distance for Mn_2 has been presented. We analysed in detail the electronic occupation of the 4s and 3d states and stressed the differences between the F and AF states. We find that the magnetic coupling depends very sensitively on the interatomic distance. For short distances the ground state is antiferromagnetic but it changes to ferromagnetic at $d = 3.06$ Å. In particular in our calculation the ground state is antiferromagnetic with an interatomic distance $d = 2.89$ Å.

The calculation was performed by assuming collinear, ferro and antiferro, and noncollinear arrangement between spins within the framework of the *ab initio* SIESTA code[37]. The basis set used for the present work to describe the valence states is a double-ζ set with a confining energy shift of 50 meV. A more detailed discussion is presented in ref. 14.

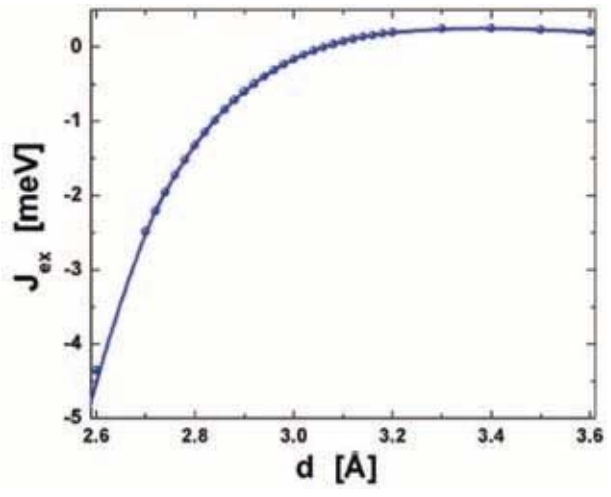

Figure 7. Exchange coupling for Mn_2 as a function of dimer distance.

These results suggest that a remarkable competition between kinetic and exchange-correlation energies leads to almost degenerate spin configurations. We obtain that the correlation energy favours antiferromagnetic behaviour for short distances, while for larger atomic separations the correlation energy of the ferromagnetic state makes it the most stable. Due to this effect, one should not expect a clear, unique, magnetic ordering in small clusters. The scenario gets more complicated in larger clusters where manganese atoms may be located at distances that favour FM or AF coupling. This competition may be the reason for the complex behaviour of manganese.

Manganese clusters

The evolution of magnetism from the atom to the bulk constitutes a fundamental problem of basic and applied physics, and its correct description is indispensable for the understanding of magnetism at the nanoscale. As mentioned above, recently, a particularly exotic behaviour of the magnetic moments as a function of size was experimentally found for Mn_n clusters[4,5], which poses a challenging problem. In ref. 14 we presented a possible theoretical description of these findings.

Consistently with the remarkable properties of Mn-compounds mentioned in the previous section, and despite the similar magnetic ordering of Mn_2 and Mn-bulk, experiments show that small manganese clusters exhibit an intriguing magnetic behaviour, with signatures of super paramagnetism and magnetic moments $\mu(n)$ smaller than 1.5 μ_B per atom[4,5,22,23,40]. The behaviour of $\mu(n)$ as a function of n is strongly non-monotonous[4,5].

In the last years, different theoretical determinations of the magnetic and electronic structure of Mn_n clusters have been reported[30,31,33,41]. Almost all calculations have in common the assumption of collinear spins, but give contradictory results. A careful analysis within an all-electron scheme came to the conclusion that Mn_2 exhibit multiple magnetic and structural minima[30].

The experimental evidence and the theoretical works mentioned above suggest that the most probable scenario for small Mn clusters is that of almost degenerate different spin configurations. Therefore, the correct approach to describe their magnetic structure must give up the assumption of collinearity. This was confirmed recently by a calculation which yields a noncollinear magnetic configuration[33] for Mn_6. Moreover, the fact that the ferromagnetic and antiferromagnetic solutions are very close in energy, in particular for very small clusters[31] could also lead to spin frustration in larger clusters. Moreover, the overall size dependence of $\mu(n)$ measured by Knickelbein[4,5] remained unexplained.

Model and calculation

We performed first a noncollinear *ab initio* determination of the magnetic properties of small Mn_n clusters on the range $2 \le n \le 8$. Our results suggest that in small Mn_n clusters a remarkable competition between kinetic and exchange-correlation energies leads to almost degenerate spin configurations which result in the formation of noncollinear magnetic nano-domains in order to avoid spin frustration. Moreover, with the help of the data obtained from the *ab initio* calculations we fit the parameters of an effective spin-Hamiltonian, which we use to calculate $\mu(n)$ for larger clusters ($9 \le n \le 40$). This model gives very good agreement with the puzzling experimental results.

To determine the electronic and magnetic properties of the clusters in the range $2 \le n \le 8$ we have used the same (SIESTA) code[37] used for the dimer case. We included spin polarization, both collinear and noncollinear[38], in the local-density approximation (LDA). The basis set used to describe the valence states is a double-ζ set with a confining energy shift of 50 meV.

The calculations have been performed in the following way. First, the clusters were completely relaxed with respect to their ionic and electronic degrees of freedom, assuming a given magnetic configuration (ferro- or antiferromagnetic) and different structural geometries. Once the ground-state geometry was obtained, we included the spin orientation of the individual atoms as additional degrees of freedom and minimized again the whole set of variables. Different calculations with different initial spin configurations have been performed to avoid trapping into local energy minima.

Results

In Figure 8 we show the ground-state structures and spin configurations obtained from the *ab initio* calculations. Interestingly, most of these clusters, in particular $n = 6$, 7 and 8, show noncollinear magnetic behaviour. This indicates that previous theoretical studies, with the exception of ref. 33, missed an essential ingredient for the correct physical description of these systems. As can be seen from Figure 8, some of the clusters show a marked Jahn–Teller distortion, like Mn_3 and Mn_4. As a general rule, the average magnetic moment μ of these clusters is at least two times smaller than the moment of an isolated Mn atom. The average magnetic moments obtained are: $\mu(2) = 0$, $\mu(3) = 1.67\ \mu_B$, $\mu(4) = 2.5\ \mu_B$, $\mu(5) = 1.0\ \mu_B$, $\mu(6) = 0.87\ \mu_B$, $\mu(7) = 0.99\ \mu_B$ and $\mu(8) = 1.17\ \mu_B$. Note that the lowest energy structure of Mn_5 corresponds to an almost bipyramidal configuration. However, symmetry is broken due to the formation of domains. A similar effect is present for $n = 6$, 7 and 8. Apart from the noncollinear behaviour, the most important feature of the magnetic configurations shown in Figure 8 is that manganese atoms separated by short distances are mostly coupled antiferromagnetically, whereas for long interatomic distances the coupling is mostly ferromagnetic. This remarkable effect, discussed in the previous section for dimers, leads to spin frustration and the formation of noncollinear nanodomains, as clearly shown in Figure 8.

In order to understand the origin of the noncollinearity and quantify its strength, we have also calculated the cohesive energies of the ferromagnetic and antiferromagnetic configurations in the ground-state geometries, assuming collinear arrangements. In Table 1, we show the energy differences between the noncollinear ground-states and the energies obtained assuming collinear spins for the same geometries. Note that for all sizes considered the energy difference between the noncollinear and the collinear arrangements is very small. This is consistent with the multiplicity of minima obtained in previous collinear theoretical studies[30]. Furthermore, the energy differences

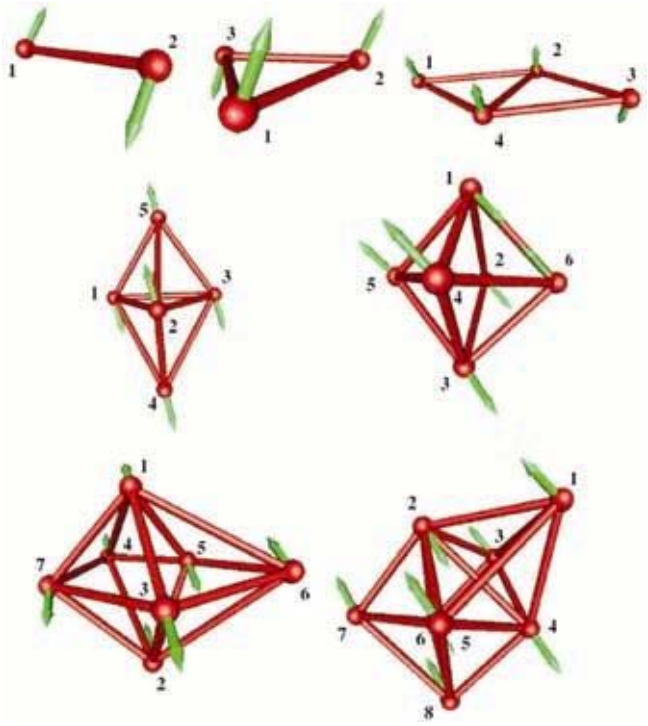

Figure 8. Ground-state structures of Mn_n clusters, for $n = 2$–8, optimized with respect to the electronic, ionic and spin degrees of freedom. The magnitude and orientation of the quantum expectation value of the spin at each atom is indicated by arrows.

Table 1. Energy differences (in meV) of the collinear and noncollinear magnetic configurations of Mn_n clusters with respect to the structure with the lowest energy

	Mn_2	Mn_3	Mn_4	Mn_5	Mn_6	Mn_7	Mn_8
ΔE_{AF}	0	16	21	1	85.5	118	43
ΔE_{FM}	10	46	21	505	564	1624	43
ΔE_{NC}	0	0	0	0	0	0	0

$\Delta E = E_{AF} - E_{FM}$ between AF and the FM configurations is also very small. The origin of this behaviour is that the different terms involved in ΔE, from whose competition the magnetic behaviour arises, almost cancel themselves in Mn, as we discuss below in detail.

In fact, the nature of magnetism in small Mn_n clusters can be inferred from the magnetic behaviour in the dimer. Although almost all *ab initio* studies performed so far for Mn_2 obtained a FM configuration, our calculations yield an AF state, with a bond length of $r_0 = 2.890$ Å. As mentioned above, this result for the magnetic ordering of the dimer is in agreement with the existing experimental evidences[23,24]. However, it must be pointed out that the FM, AF and noncollinear states are almost degenerate (see Table 1).

Now, and in order to determine the magnetic properties of clusters with n up to 40, which cannot be done yet using *ab initio* approaches we propose an effective spin Hamiltonian of the form

$$H = \sum_{\substack{i,j=1,n \\ i \neq j}}^{n} J_{ij} \vec{S}_i \cdot \vec{S}_j + V(\{|\vec{r}_i - \vec{r}_j|\}), \quad (2)$$

where the $\vec{S}_i$ are classical spins, with magnitudes measured in Bohr magnetons. The exchange coupling constants J_{ij} are the distance-dependent quantities $J(|\vec{r}_i - \vec{r}_j|)$, being $|\vec{r}_i - \vec{r}_j|$ the distance between atoms i and j. We use for $J(|\vec{r}_i - \vec{r}_j|)$ the function $J(d)$ extracted from the dimer.

Moreover, we analysed carefully the local magnetic moments S_i obtained from the *ab initio* calculations (Mn_2 to Mn_8) as a function of the coordination number z, and we obtained a clear relation between them. It turns out that a function of the form $S = 4.42 - 0.5z$ for $z \leq 8$ and $S_i = 0.4$ for $z > 8$, reproduces the results obtained for small clusters. The coordination number z_i of atom i is defined as the number of neighbours being at a distance smaller than 2.26 Å (nearest neighbour distance in bulk-Mn) from atom i. It must be pointed out that, although the spins $\vec{S}_i$ are treated as classical, the scalar product is taken into account. Therefore, the Hamiltonian H intrinsically includes noncollinearity. Note that the approximation of classical spins is justified by the high local moments of Mn, and is also used for the description of manganites[21]. In eq. (2), $V(\{|\vec{r}_i - \vec{r}_j|\})$ is, in general, a many-body potential which models the cohesive energy of the cluster. For simplicity, we take a Lennard–Jones–(LJ) type potential to generate compact structures, which are expected for cluster in the size range we are interested in. Since we seek for a qualitative explanation of the size dependence of the magnetic properties of these clusters, a simple LJ potential should work reasonably well for our purposes. We minimized H numerically, by using genetic algorithms, and obtained the ground state spin-configurations for clusters up to Mn_{40}. The calculated size dependence of the magnetic moments per atom is shown in Figure 9, where we also show the *ab initio* results. Clearly, the orders of magnitude of the all calculated magnetic moments are in good agreement with experiment. Moreover, the overall size dependence $\mu(n)$ is well described and shows a complex behaviour, as in the experiment[4,5]. Note that in our results the oscillations as a function of n between $n = 6$ and $n = 13$, $n = 14$ and $n = 20$, and between $n = 21$ and $n = 31$, observed in experiment are very well reproduced.

In Figure 9 we also show the magnetic moments of isomers of Mn_{13}, Mn_{14} and Mn_{15} which have smaller cohesive energy than the ground-state structures, but which might also be present in the cluster beam on which experiments have been performed. The good agreement between our model and experiment indicates that the physics underlying our model is correct, i.e. the magnetic properties of Mn_n clusters are dominated by spin frustration due to the presence of different spin–spin coupling constants, which leads to noncollinear magnetism and formation of nanodomains. As a consequence, $\mu(n)$ shows a complex form and low magnetic moments, which reect the least frustrated possible spin configurations.

Conclusion and summary

Summarizing, we present an explanation for the puzzling behaviour of $\mu(n)$ for Mn_n clusters up to $n = 40$. Note that the experimentally obtained $\mu(n)$ shows a further oscillation between $n \sim 40$ and 80. We believe that this feature is due to the interplay between structure and magnetism. For those sizes, the cluster structure tends to acquire

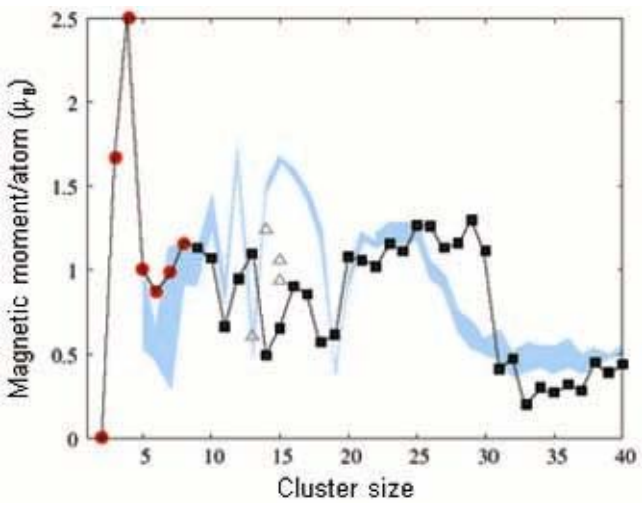

Figure 9. Size dependence of the magnetic moment per atom μ (in units of μ_B) of Mn_n clusters in the size range $2 \leq n \leq 40$. Red circles correspond to the *ab initio* results. Squares show the calculated μ for compact structures using the classical spin-Hamiltonian of eq. (2). Grey open triangles refer to isomers having smaller cohesive energies. The light-blue shadowed zone corresponds to the experimental results of refs 4 and 5 taken into account the reported error bars.

some signatures of α-Mn. On the other hand, the ferromagnetic coupling is still present. Thus, a competition between cohesion and magnetic energy takes place. Between $n \sim 40$ and 80 the magnetic energy seems to dominate. According to this idea, for clusters with $n > 80$ the structures should slowly converge to the bulk one and the magnetic ordering approach the AF state of α-Mn. In order to describe such a competition, a more accurate description of $V(\{|\vec{r}_i - \vec{r}_j|\})$ is needed.

Cobalt nanowires

As mentioned in the introduction, nanowires of transition metals are some of the most studied systems. A rich variety of applications make them attractive. Of course, revealing the precise correlation between the measured data and both the microscopic, geometrical and chemical features, is a fundamental issue (for both basic research and applied science) that need to be addressed to achieve with success the possible applications of these kind of nanostructures in the magnetic recording technology and in the design of novel spintronic devices.

Interestingly, the structural characterization of electrodeposited nanowires has revealed that their atomic configuration strongly depends on the synthetic protocol and, in this sense, the case of cobalt is the most illustrative. Actually, with the help of X-ray diffraction patterns as well as of both scanning and transmission electron microscopy images, it has been obtained for example that the as synthesized Co nanowires: (i) are in fact composed of several nanometer-sized grains having different geometrical phases, sizes, and relative orientations[7–9,42], (ii) that they are not perfectly aligned[7,8,42] (i.e. it has been found that the angle between the wire axis and the normal to the film plane ranges typically between 0 and 30 degrees), and that (iii) their cross section is not uniform all along the length of the wires, leading in some cases to constrictions and to significant deviations from the cylindrical shape[42,43]. On the one hand, it is clear that the previous complex atomic organization of the wires within the pores is expected to have a strong influence on the measured macroscopic response of the samples and, on the other hand, their precise characterization is of course necessary also to adequately model their magnetic and electronic properties.

In this respect, a large amount of theoretical work has been reported in the last years in which mainly phenomenological approaches have been used to model very complex microscopic phenomena that occur in these kind of systems like, for example, magnetization reversal mechanisms[12,42,44], the role played by the wire packing density and magneto-static interactions[45], as well as the domain wall motion within the wires[46]. In general, in these cases, the wires are mainly modelled as uniform assemblies of structureless cylinders or as chains of spheres or ellipsoids. However, despite the use of these simplified conditions, from these calculations it has been possible to elucidate interesting mechanisms that could be at the origin of experimentally measured magnetoresitance data and the behaviour of magnetostatic interactions in ordered nanowire arrays. Of course, it is clear that simple models are a necessary requirement for massive simulations involving an assembly of wires of realistic size. However, it is reasonable to expect more accurate results (or the appearance of new phenomena) by taking into account the electronic structure of the species involved, as well as, the precise geometrical details of the wires.

At this point, it is important to comment that more accurate semiempirical tight binding (TB) studies and density functional theory (DFT) calculations have been mainly restricted to analyse the structural and magnetic properties of nanowires in the form of deposited[47–52] or free standing systems[53–55]. In the former, monoatomic chains of different lengths and chemical compositions have been deposited on both perfectly at and stepped surfaces and interesting trends concerning their structure and magnetic configuration have been revealed. Furthermore, with the inclusion of the spin–orbit (SO) interaction in the model Hamiltonians, it has been possible to qualitatively estimate the role played by the magnetization direction on the transport properties of the wires[56] as well as the values of the orbital moments in these kind of one-dimensional structures[49,50,55]. In addition, the calculation of the magnetocrystalline anisotropy energy (MAE) has been particularly extensively addressed in the literature since it determines, via the SO interaction (which connects the spin moment to the atomic structure of a magnetic material) the low energy orientation of the magnetization within the structures[50,51,53–55]. However, despite the large amount of studies reported in the last years little is known, to the best of our knowledge, about the influence of more realistic geometrical imperfections like polycrystallinity, finite size effects, and the presence of internal defects in the magnetic properties of transition metal nanowires, particularly on the basis of an electronic theory.

In this part we present some of the systematic theoretical investigation[67] dedicated to analyse the magnetic properties of finite length Co nanowires with complex atomic configurations and having an aspect ratio that varies in the x–y range. We use a d-band tight-binding Hamiltonian treated in the unrestricted Hartree–Fock approximation, where the effects of the SO interaction (which allows us to calculate the orbital moment contributions to the total magnetization as well as the magnetic anisotropy energy) are included non-perturbatively.

As already commented above, cobalt was chosen because of its wide technological applications and rich nanometric behaviour. Concerning the geometrical structure of our nanowires we consider, (i) monoatomic chains and (ii) polycrystalline atomic configurations (guided by experimental results)[7–9,42]. The latter being characterized by the

presence of various fcc and hcp grains of different sizes which are stacked together to form metallic wires with contrasting surface terminations and with several internal interfaces.

In all cases, we consider two directions of the magnetization δ within the structures oriented along ($\delta = x$) and perpendicular ($\delta = z$) to the wire axis. We show that it is possible to obtain sizable variations in the magnitude and sign of the magnetic anisotropy energy (leading to strong oscillations of the easy axis between parallel and perpendicular directions) when the length of the wire increases, as well as, when the geometrical details of the wire-ends or the internal structure are modified. As far as the electronic structure is concerned, we show also that there is a strong dependence of the density of states on the magnetization direction and microstructure of the wires, consisting in sizable energy shifts and changes in the degeneracy of the eigenvalues, a result that is expected to strongly modify the number and orbital nature of the conduction channels in the structures.

Method of calculation

Self-consistent semiempirical calculations have been performed for several Co nanowires by using the realistic *d*-band tight-binding Hamiltonian, proposed in ref. 58, which includes the intra-atomic Coulomb interactions in the unrestricted Hartree–Fock approximation and the effects of the SO coupling nonperturbatively. The model has been described in detail elsewhere[59,60], thus we only summarize its main points and discuss the choice of parameters.

Due to the inclusion of the SO interaction, the rotational invariance of the electronic Hamiltonian is no longer preserved and depends now on the orientation δ of the magnetization in the system. In the usual notation the Hamiltonian is given by

$$H^{\delta} = \sum_{i\lambda,\sigma} \Delta\varepsilon^{\delta}_{i\sigma} n_{i\lambda\sigma} + \sum_{i\lambda,j\mu,i\neq j,\sigma} t_{i\lambda,j\mu} c^{+}_{i\lambda\sigma} c_{j\mu\sigma} + \sum_{i,\lambda\sigma,\mu\sigma'} \xi(\vec{L}_i \cdot \vec{S}_i)_{\lambda\sigma,\mu\sigma'} c^{+}_{i\lambda\sigma} c_{i\mu\sigma'}, \quad (3)$$

where $c^{+}_{i\lambda\sigma}$ ($c_{i\lambda\sigma}$) refers to the creation (annihilation) operator of an electron with spin σ in the *d* orbital λ at atomic site *i* and $n_{i\lambda\sigma} = c^{+}_{i\lambda\sigma} c_{i\lambda\sigma}$ defines the electron number operator. The first term of eq. (3), $\Delta\varepsilon^{\delta}_{i\sigma}$ corresponds to the site- and spin-dependent energy shift of the *d* level $\varepsilon_{i\sigma} = \varepsilon^{0}_{d} + \Delta\varepsilon^{\delta}_{i\sigma}$ (where ε^{0}_{i} stands for the *d* orbital energy in the paramagnetic bulk) and is determined by the global charge and the spin as follows

$$\Delta\varepsilon^{\delta}_{i\sigma} = U(i)\Delta n^{\delta}(i) - \sigma J(i) S_{\delta}(i), \quad (4)$$

with $\Delta n^{\delta}(i) = n^{\delta}(i) - n_d(\text{bulk})$. The average intra-atomic direct Coulomb repulsion integral is denoted by *U* and the average exchange integral is denoted by *J*. The spin-quantization axis is taken to be parallel to the magnetization direction, which is assumed to be uniform within the wires. In the second term of eq. (3), $t_{i\lambda,j\mu}$ denotes the corresponding hopping integrals between sites *i* and *j* and orbitals λ and μ and finally, the third term corresponds to the SO interaction treated in the usual intra-atomic single-site approximation[61,62]. Here, ξ stands for the SO coupling constant and $(\vec{L}_i \cdot \vec{S})_{\lambda\sigma,\mu\sigma'}$ refers to the intra-atomic matrix elements of $\vec{L} \cdot \vec{S}$ which couple the up and down spin-manifolds and which depend on the relative orientation between the magnetization direction and the wire lattice. The number of *d*-electrons at site *i*,

$$n^{\delta}(i) = \sum_{\lambda} (\langle n^{\delta}_{i\lambda\uparrow} \rangle + \langle n^{\delta}_{i\lambda\downarrow} \rangle), \quad (5)$$

and the local spin $\vec{S}(i) = [S_x(i), S_y(i), S_z(i)]$ at each cluster site *i* and for a given direction of magnetization δ,

$$S_{\delta}(i) = \frac{1}{2} \sum_{\lambda} (\langle n^{\delta}_{i\lambda\uparrow} \rangle - \langle n^{\delta}_{i\lambda\downarrow} \rangle), \quad (6)$$

are calculated self-consistently by integrating the local density of states (LDOS) $\rho^{\delta}_{i\lambda\sigma}(\varepsilon) = -(1/\pi)\text{Im}\{G^{\delta}_{i\lambda\sigma,i\lambda\sigma}(\varepsilon)\}$, where $G^{\delta}(\varepsilon) = [\varepsilon - H^{\delta}]^{-1}$ is the Green function operator, up to the Fermi level ε_F which is determined by the number of *d* electrons per atom in the wires.

The local orbital moments $L_{\delta}(i)$ at each wire site are calculated from

$$L_{\delta}(i) = \sum_{\sigma} \sum_{m=-2}^{m=2} \int_{-\infty}^{\varepsilon_F} m \rho^{\delta}_{im\sigma}(\varepsilon) \mathrm{d}\varepsilon, \quad (7)$$

where the real *d*-orbitals have been transformed to the complex spherical harmonics basis and *m* refers to the magnetic quantum number. Here, the quantization axis of the orbital momentum is the same as the spin quantization axis.

The electronic energy $E_{\delta} = \sum_i E_{\delta}(i)$ can be written as the sum of local contributions

$$E_{\delta}(i) = \sum_{\lambda\sigma} \left[\int_{-\infty}^{\varepsilon_F} \varepsilon \rho^{\delta}_{i\lambda\sigma}(\varepsilon) \mathrm{d}\varepsilon - E^{dc}_{i\lambda\sigma} \right], \quad (8)$$

corresponding to the different atoms *i* within the wires and where $E^{dc}_{i\lambda\sigma}$ stands for the double-counting correction.

The magnetocrystalline anisotropic energy (MAE) is defined as the change ΔE in the electronic energy E_{δ} associated with a change in the orientation of the magnetization. In this work we consider, for each cobalt nanowire, two directions of the magnetization δ being oriented along ($\delta = x$) and perpendicular ($\delta = z$) to the wire axis. However, it is important to comment that the magnetization direction can be chosen without restrictions. Actu-

ally, taking advantage of our local approach it is possible to express the total energy difference ΔE_{xz} between two arbitrary orientations $\delta = x$, z as a sum of atom resolved contributions:

$$\Delta E_{xz} = \sum_i \Delta E_{xz}(i) = \sum_i [E_x(i) - E_z(i)], \quad (9)$$

where $E_\delta(i)$ is given by eq. (8). Thus global the magnetoanisotopic properties can be related to the various local atomic environments within the wires. The LDOS $\rho^{\delta}_{i\lambda\sigma}(\varepsilon)$ are determined by performing independent self-consistent calculations for each orientation of the magnetization δ by using Haydock–Heine–Kelly recursion method[63] and in this way we derive the MAE in a nonperturbative fashion as difference between electronic energies.

Results and discussion

In this subsection, we present the local atomic environment dependence of both spin and orbital magnetic moments, as well as of the MAE, together with the resulting low energy orientations of the magnetization within our considered cobalt nanowires. The parameters used for the calculations are obtained from bulk properties: *d*-band width, equilibrium distance, and bulk magnetic moment as follows. The two-centre d electron hopping integrals ($dd\sigma$, $dd\pi$, $dd\delta$) are defined by the canonical expressions given by Heine[64], varying as the inverse fifth power of the interatomic distance r: $dd\sigma = -6(W_b = 2/5)(r_{WS} = r)^5$, $dd\pi = 4(W_b = 2.5)(r_{WS}/r)^5$ and $dd\delta = -1(W_b = 2.5)\ (r_{WS}/r)^5$ in terms of the corresponding bulk *d*-band width[65] of Co, W_b(Co) = 5.5 eV and the Wigner-Seitz radius r_{WS}. Charge transfer effects are treated in the limit of large direct Coulomb repulsion $U(i)$ [i.e. $U(i) \to +\infty$ and $\Delta n(i) \to 0$ with $U(i)\Delta n(i)$ finite], which amounts to impose local charge neutrality at each site i. The values for the *d*-band filling n_d(Co) = 8.3 and intra-atomic exchange integral J_{Co} = 0.76 eV (fitted to reproduce the proper magnetic moment and exchange splitting in the bulk), as well as the SO-coupling constant ξ_{Co} = 88 meV (obtained from ref. 62), have been already used in previous works[15,59,66].

Magnetic properties of Co monoatomic chains. We study first the magnetic properties of finite length monoatomic Co chains. We consider two directions of the magnetization oriented along ($\delta = x$) and perpendicular ($\delta = z$) to the wire axis, and we use a fixed nearest neighbour interatomic distance between Co atoms, being equal to R_o = 2.44 Å (which corresponds to the value in the bulk phase).

In all our considered wires we have found that the modulus of the spin moment $|\vec{S}|$ depends very weakly on the direction of magnetization δ, therefore, for each one of our considered atomic chains, we will only refer to the results for $2S_z$. Actually, in addition to this weak dependence on δ, we have found also in all our one-dimensional structures almost saturated local spin moments $2S_z(i) \sim 1.7\ \mu_B$ in all the sites i and, as a consequence, $2S_z$ is not so sensitive either to the local atomic environment or to the length l of the chains. This behaviour is characteristic of magnetic nanostructures defined by a large exchange regime and has been also found in various types of magnetic systems such as in TM clusters having different sizes and symmetries[66,68], as well as in magnetic thin films with different packing[69].

However, in contrast to the almost constant dependence of the spin moments on δ, i and l, we see from Figure 10 that the local orbital magnetic moments $L_\delta(i)$ for Co_{19} (Figure 10 *a*), Co_{49} (Figure 10 *b*) and Co_{89} (Figure 10 *c*) wires (shown as representative examples) are more sensitive to variations in the direction of the magnetization and in the local atomic environment. From the figure we note first that very enhanced values for $L_\delta(i)$, with respect to the hcp Co bulk (marked with an horizontal dashed line) are found in all our chains, the largest enhancement being obtained in general at the sites located at the end of the wires where $L_\delta(i) \sim 1\ \mu_B$. However, notice that a sizable part of this increase in the local orbital moments is considerably lost when we move to the inner regions of the atomic chains, where $L_\delta(i)$ decays very fast (with some oscillations) with increasing the distance from

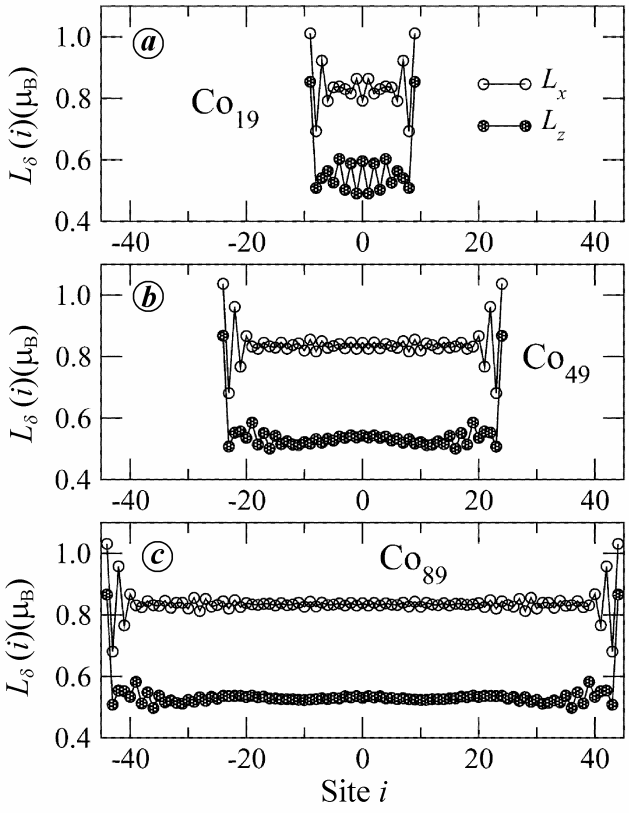

Figure 10. Calculated local orbital moments $L_\delta(i)$ (μ_B) for (***a***) Co_{19}, (***b***) Co_{49}, and (***c***) Co_{89} monoatomic wires.

the extremes of the chains. Interestingly, we observe in all our considered wires almost the same value for $L_\delta(i)$ at the centre of the structures, being of the order of 0.5 μ_B for $\delta = z$ and of 0.8 μ_B for $\delta = x$. These values could be representative of the infinite chain limit and, actually, they are very close to the ones calculated by Komelj *et al.*[49] for monoatomic Co wires by means of *ab initio* techniques, a fact that give us confidence in our results.

It is important to comment also about the difference $L_z(i) - L_x(i) = \Delta L_{zx}$, of the calculated local orbital moments in each site i between the two different orientations of the magnetization. From Figure 10 we note also that sizable values for ΔL_{zx} vs i are found, being as large as 0.4 μ_B (at the sites located at the wire ends), and which are orders of magnitude larger than the values for ΔL_{zx} previously found at magnetic transition metal surfaces[59] and nanoparticles[67]. It is important to precise that the magnitude and sign of ΔL_{zx} is particularly relevant due to the well-known (second-order perturbation theory) expression that relates both the anisotropy in the orbital moments with the anisotropy in the electronic energies through the proportionality equation $L_z - L_x \propto E_x - E_z$[62]. This relation implies that the easy axis in the systems can be also inferred by determining (e.g. by means of X-ray magnetic circular dichroism experiments[70]) the direction of magnetization δ characterized by the largest value of the orbital moment. Following these arguments, we can thus clearly predict from Figure 10 that the direction $\delta = x$ will define the low-energy orientation of magnetization in all our considered monoatomic wires.

In fact, this is what we observe from Figure 11 where we plot the average magnetic anisotropy energy, $\langle \Delta E_{xz} \rangle$ as a function of the length of our considered chains calculated by eq. (9). From the figure we clearly see that, in all cases, sizable negative values for $\langle \Delta E_{xz} \rangle$ are found, a fact that implies that the low energy direction of the magnetization is oriented along the wire axis in agreement with the orbital magnetization data shown in Figure 10. This result is also consistent with previous calculations reported in ref. 51 for both finite and infinite monoatomic Co chains where a highly stable magnetization direction along the wires axis was found. In addition, in that work it was clearly shown that the interaction of Co chains with a Pd surface could strongly perturb their magnetic properties, being at the origin of spin reorientation transitions in the systems. However, we believe that the here-reported trends are expected to hold in the case of weakly interacting substrates (i.e. negligible charge transfer), such as insulating films or semiconducting surfaces, where only sizable perturbations in the nearest neighbour interatomic distance between the Co atoms in the deposited chains are expected to occur. In fact, to analyse these structural effects we have performed additional calculations to study the magnetic properties of more realistic strained Co monoatomic wires.

We have chosen the Co_{19}, Co_{49} and Co_{89} chains (already analysed in Figure 10) as representative examples and, in all cases, we have found that uniform contractions or expansions in the Co–Co bond length, at least as large as 5%, are not enough to change the low energy direction of the magnetization calculated in Figure 11, defining as a consequence a highly stable spin orientation in the systems.

In ref. 15 we analysed also the magnetic properties of finite-length single-crystal fcc nanowires as the ones shown in Figure 12. These cylindrical structures are compact portions of the fcc lattice grown along the (111) di-

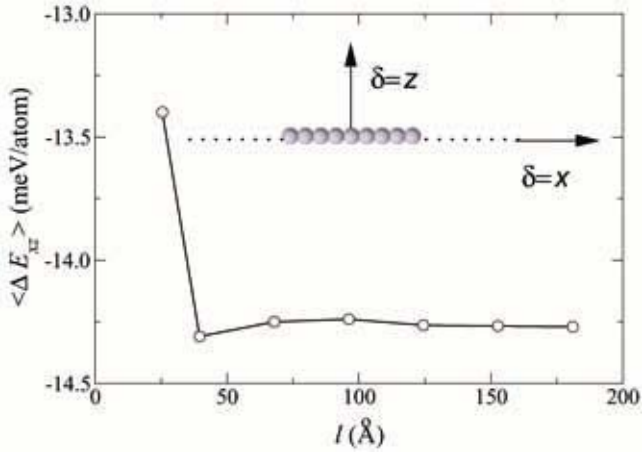

Figure 11. Average magnetic anisotropy energy, $\langle \Delta E_{xz} \rangle$ (meV/atom), calculated for our considered monoatomic wires as a function of their length l (Å). Two magnetization directions are shown in the inset.

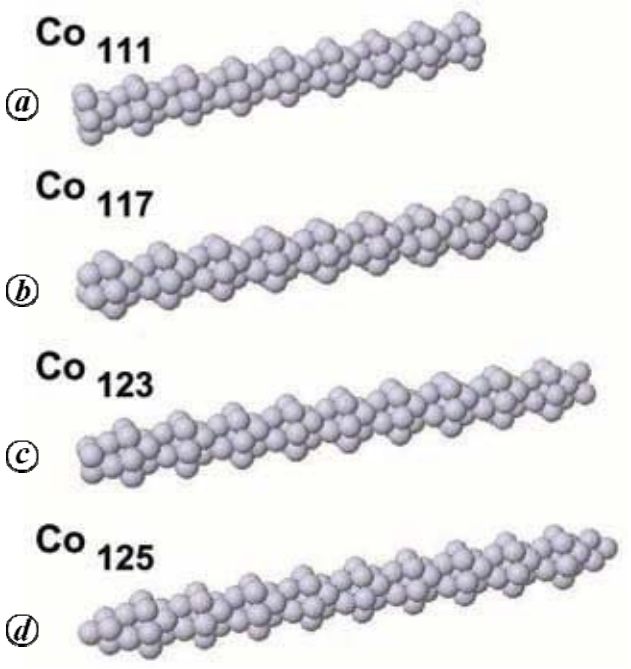

Figure 12. Illustration of our considered single crystal fcc nanowires grown along the (111) direction for (***a***) Co_{111}, (***b***) Co_{117}, (***c***) Co_{123} and (***d***) Co_{125}.

rection. In the figure, we show as representative examples the wire structures for Co_{111} (Figure 12 *a*), Co_{117} (Figure 12 *b*), Co_{123} (Figure 12 *c*) and Co_{125} (Figure 12 *d*). They are all formed by a central atomic chain placed along the *x*-axis surrounded by two successive coaxial shells (made of triangular and hexagonal units), resulting in ultra-thin wire structures with an average diameter equal to 3.9 Å. Notice from the figure that nanowires of different lengths can also differ in the atomic structure of their wire-ends a fact that, play a fundamental role in determining the average magneto-anisotropic behaviour in the systems.

Magnetic properties of polycrystalline Co nanowires. In this section we present the magnetic properties of finite-length polycrystalline Co nanowires. Some of our considered polycrystalline structures are shown in Figure 13 and are characterized by the presence of various fcc and hcp grains of different sizes, grown along the (111) and *z*-directions respectively, which are stacked together to form metallic wires with contrasting surface terminations and with several internal interfaces. In Figure 13 *a* we show first the structure of a single fcc wire made of 195 atoms. In Figure 13 *b* we show the case of a Co nanowire having 183 atoms and made of three fcc fragments, each one of them having a length $l = 24.8$ Å. These fragments are attached together through the hexagonal units (as marked in the figure) and are rotated with respect to each other by 30 degrees. Notice that, when comparing with the single crystal wire shown in Figure 13 *a*, the different relative orientation between the segments leads to the formation of a Co nanowire with a more corrugated surface.

In Figure 13 *c* we present a Co cylindrical structure in which the central region of the nanowire is made of a cylindrical fcc fragment to which we add, in both sides, an hcp grain having 80 atoms and a length of 30.4 Å. As marked in the figure, the two types of structures are attached through a junction involving a triangular cluster and an hexagonal unit. In Figure 13 *d*, a similar type of construction is presented but now the hcp fragment is the one located in the centre of the wire and the fcc fragments are found to be attached to the left and to the right of the hcp cylindrical segment. Notice that, when comparing with the single crystal structure shown in Figure 13 *a*, all our considered polycrystalline wires are approximately of the same length (varying by ±8 Å) but strongly differ in their microstructure. Finally, it is important to comment that even if the previous type of constructions roughly model the structural features reported for this kind of systems[7–9,42], we believe that our here-proposed atomic configurations contain the fundamental ingredients necessary to analyse the changes in the local magnetic moments and MAE values due to the existence of a non-perfect growth.

In Figure 14, we show our results for the calculated average magnetic anisotropy energy, $\langle \Delta E_{xz} \rangle$, for some representative polycrystalline Co nanowires. We include also

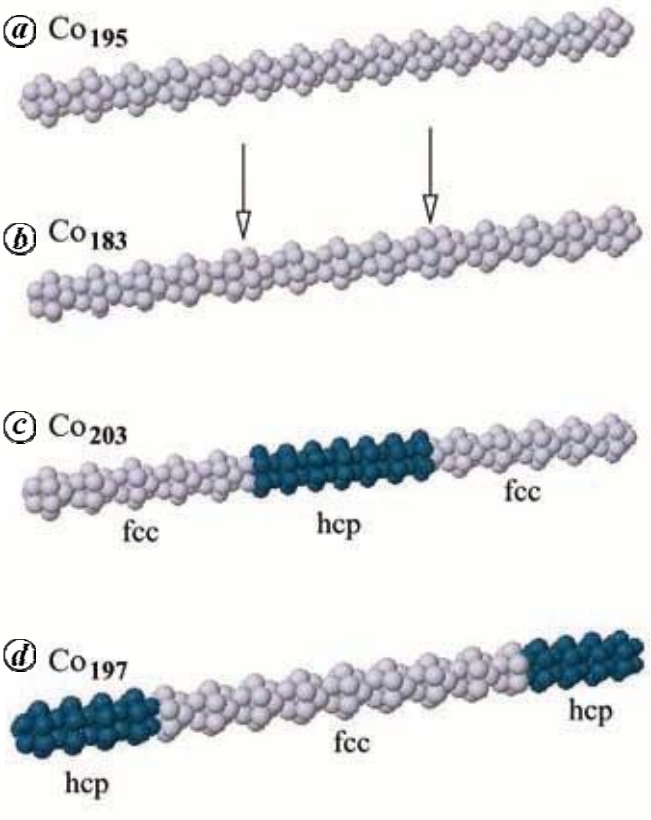

Figure 13. Illustration of our considered polycrystalline Co nanowires. ***a***, A single fcc Co_{195} structure grown along the (111) direction; ***b***, Co_{183} wire composed of three fcc segments rotated with respect to each other by 30 degrees, being attached through hexagonal units; ***c***, A polycrystalline Co_{203} nanowire made by a central hcp fragment (blue spheres) to which we attach in both sides an fcc portion (gray spheres); ***d***, A polycrystalline Co_{197} structure made by a central fcc fragment (gray spheres) to which we attach in both sides an hcp portion (blue spheres).

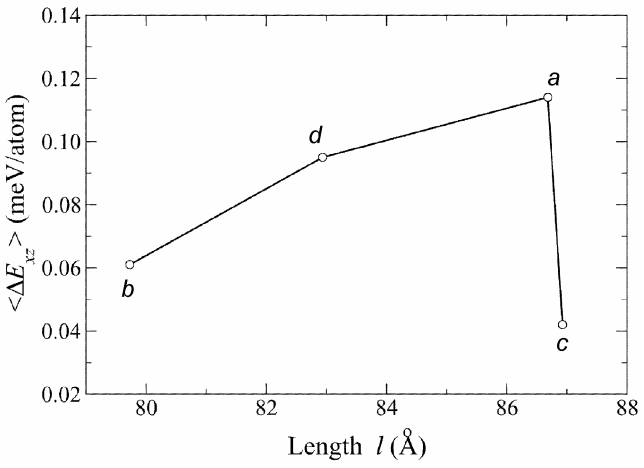

Figure 14. Average magnetic anisotropy energy, $\langle \Delta E_{xz} \rangle$ (meV/atom), calculated for the wire structures shown in Figure 13.

in the figure, and for the sake of comparison, our calculated value for $\langle \Delta E_{xz} \rangle$ for the single crystal atomic configuration shown in Figure 13 *a*. From the figure we see as a general trend that, when considering a grain-like structure for Co nanowires, the energy difference $\Delta E_{xz} = E_x - E_z$ between parallel and perpendicular directions of magnetization (when compared to the single crystal wire) is always reduced. This is particularly the case when both fcc and hcp phases coexist within the structures, as seen from our data shown in Figure 14 for Co_{203} with a length of 87 Å. Still, the calculated values for $\langle \Delta E_{xz} \rangle$ are larger than the ones found for bulk hcp Co ($\sim 10^{-5}$ eV). Interestingly, and in contrast to the results for single crystals[15], we notice that introducing this kind of structural imperfections does not lead to spin-reorientation transitions in the systems. However, our results shown in Figure 14 could imply that, in real samples, reducing the degree of polycrystallinity might lead to the formation of magnetic nanowires with a more stable low energy magnetization direction.

Actually, it is possible to trace the sizable reduction in the MAE values shown in Figure 14, to the already observed sensitivity of ΔE_{xz} to the local atomic environment. In particular, it will be interesting to analyse the average MAE contributions of each one of the grains, and how they combine to define the average magneto-anisotropic behaviour of the wires. In this respect, we show in Figure 15 the average MAE contributions $\langle \Delta E_{xz}(V_i) \rangle$ for well-defined volumes, V_i, for each one of the selected volumes V_i as well as the average MAE in the structures. From Figure 15 *b* we see first that by simply introducing a small degree of orientational disorder in a single crystal structure, a sizable reduction in the total MAE is obtained (compare with Figure 15 *a*). Note that, in contrast to the results shown in Figure 15 *a*, the end portions of the wires contribute now with small positive values, of the order of ~ 0.034 meV, thus dominating the global magneto-anisotropic behaviour and begin at the origin of the notable reduction in the total MAE.

From Figure 15 *c* a more interesting behaviour is observed since, besides the small and positive values obtained for $\langle \Delta E_{xz}(V_{fcc}) \rangle$ in the fcc fragments located at the extremities, the average local contribution of the hcp grain $\langle \Delta E_{xz}(V_{hcp}) \rangle$ is found to be negative, implying that the low energy direction of magnetization in this well-defined volume is oriented along the *x*-axis. Of course, these local values result in non-additive contributions that are at the origin of a more reduced MAE value as indicated in the figure. Finally, and in contrast to the results shown in Figure 15 *c*, from Figure 15 *d* we see that hcp fragments located at the wire ends have an average magnetization oriented perpendicular to the wire-axis ($\langle \Delta E_{xz}(V_{hcp}) \rangle > 0$), similar to the central fcc volume, a contribution that reinforces the spin direction perpendicular to the wire as the easy axis of the structure. Interestingly, this kind of grain-like structure has been observed in real samples of Co nanowire arrays fabricated by the electrodeposition technique[6], or appear naturally if the wires are formed through the aggregation of nanoparticles[71]. We can thus conclude by saying that a detailed characterization of the wire structure should be very important for a precise characterization of the material properties, as well as for more realistic comparisons between theory and experiments.

The role of the presence of grain boundaries on the local distribution of the orbital moments and magnetic anisotropy energies can also be analysed by plotting the average values of $\langle \Delta E_{xz} \rangle$ and $\langle L_\delta \rangle$ found for both the hexagonal and triangular units, as well as for the single Co atoms located all along the length of the wire defining different shells m ($m = 0$ being the centre of the wire). This data is plotted in Figures 16–18 for single crystal Co_{195}, as well as polycrystalline Co_{183} and Co_{203} structures, which are shown in Figures 13 *a*–*c*.

From Figure 16 *a* and *b* we see that, for the single crystal wire, a highly regular distribution for both $\langle \Delta E_{xz}(m) \rangle$ and $\langle L_\delta(m) \rangle$ as a function of m is obtained within the structure. However from Figures 17 and 18, it is interesting to remark that the previously well-defined sequence of values obtained for $\langle \Delta E_{xz}(m) \rangle$ and $\langle L_\delta(m) \rangle$ are notably perturbed, particularly in Figure 18 where different geometrical phases coexist within the wire. Notice that the local anisotropies are more strongly affected by the presence of these grain boundaries, leading to a highly non uniform $\langle \Delta E_{xz} \rangle$ vs m curve but with a more equilibrated distribution of positive and negative contributions. The previous local distribution leads to strong cancellation ef-

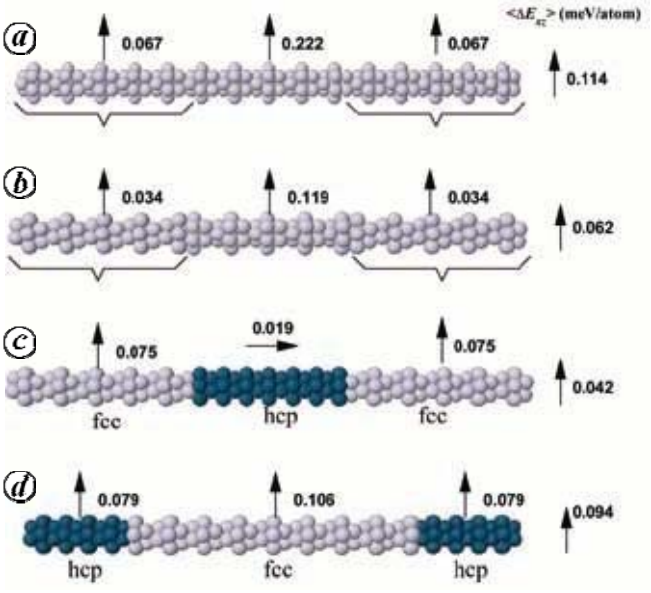

Figure 15. Calculated average magnetic anisotropy energy, $\langle \Delta E_{xz}(V_i) \rangle$ (meV/atom), for selected volumes (as indicated in the figure) for the Co nanowires shown in Figure 13. The low energy orientation of the magnetization of each fragment V_i is indicated by an arrow. To the right of each figure we show also the calculated value for $\langle \Delta E_{xz} \rangle$.

fects being thus responsible for the sizable quenching of the average MAE found in Figure 14.

We believe that the previous results obtained for both single crystal and polycrystalline Co nanowires are particularly relevant when they are set in the form of an array since the different values found for the average MAE, for the different types of microstructure, will compete or add with the other magnetic anisotropy energy contributions such as the shape anisotropy or dipolar interactions, playing thus a fundamental role in defining the average magnetic properties of the samples.

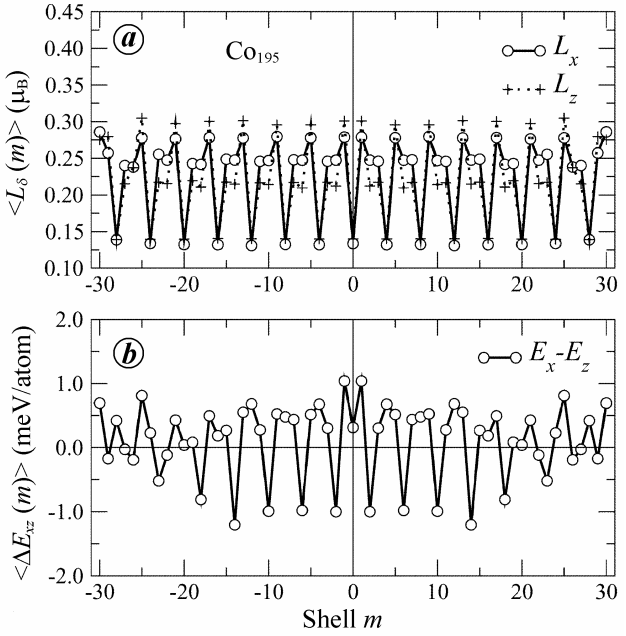

Figure 16. ***a***, Average local orbital moments, $\langle L_\delta(m)\rangle$ (μ_B), for the single crystal Co_{195} wire shown in Figure 13 *a* as a function of shell *m*; ***b***, Same as in (***a***) but for the average local magnetic anisotropy energy, $\langle\Delta\rangle$.

Calculation of the density of states

As is well known, previous theoretical works performed on transition metal clusters[53], monoatomic wires[53,54,56] and thin films[72] have shown that changing the spin orientation within the structures led to significant perturbations in their electronic spectra, consisting in sizable energy shifts as well as in changes in the degeneracy of the eigenvalues (induced by the SO coupling) occurring all along the energy level distribution. In fact, the previous electronic perturbation have been found to be of fundamental importance (when they are present around the Fermi energy) for determining the magnitude of the anisotropy barriers between two directions of magnetization as well as for explaining the spin-reorientation transitions observed in these kind of magnetic nanostructures.

In order to show these effects in our considered Co nanowires, we plot in Figures 19 and 20 the average density of states (ADOS) of single crystal Co_{195} (Figure 13 *a*) and polycrystalline Co_{183} (Figure 13b) structures respectively, for the two considered directions of magnetization, δ. From the figures we see, in both cases, a strong dependence of the ADOS on the orientation of the magnetization. As expected we found the existence of

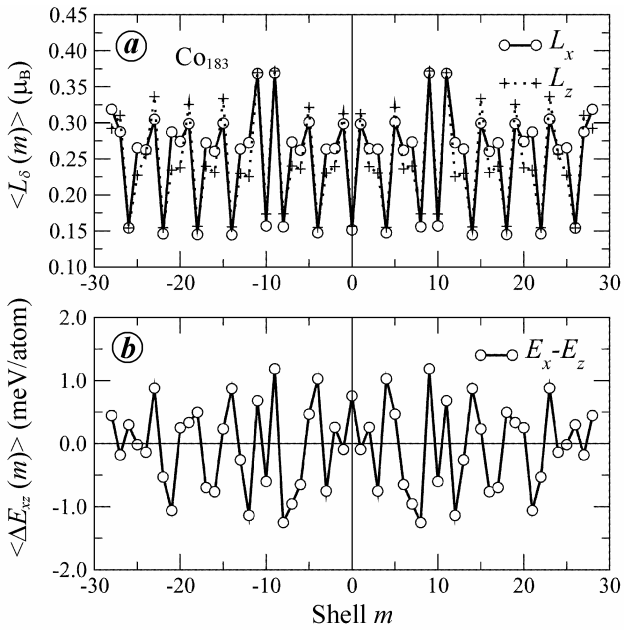

Figure 17. Same as in Figure 16 but for the Co_{183} nanowire shown in Figure 13 *b*.

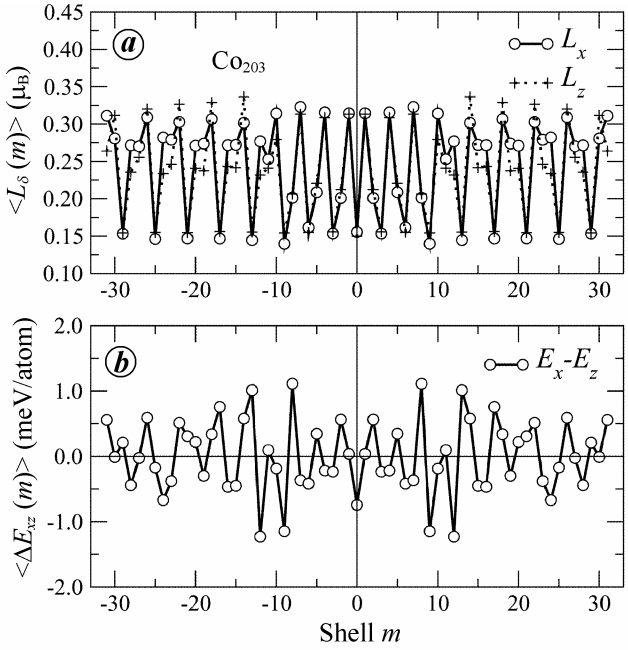

Figure 18. Same as in Figure 16 but for the Co_{203} nanowire shown in Figure 13 *a*.

sizable energy shifts and SO-coupling-induced removal of degeneracies all along the energy range. This is particularly the case of the electronic structure in the polycrystalline configuration shown in Figure 20 wherein a more abundant and less intense peak structure is observed in the ADOS for the two orientations of the magnetization. This less degenerated spectrum (which is primarily linked to the reduced symmetry of the nanowires) leads of course to a more closely spaced energy level distribution, rendering more effective the SO mixing between occupied and empty electronic states around the Fermi level.

It is clear that the previous SO-induced modifications in the eigenvalue spectra will affect other electronic properties in the material and, in particular, in the case of ferromagnetic atomic contacts, a strong dependence of the conductance on the direction of magnetization has already been found[56]. This is physically expected since, as already stated above, when the magnetization is rotated, the energy shifts of the eigenvalues as well as the band splittings obtained around the Fermi energy, will play an important role in defining the number, orbital nature, and degeneracy of the conduction channels in the wires. Of course, a direct inference of the conduction from the structure of the ADOS shown in Figures 19 and 20 is not possible but these quantities are intimately linked. In any case it is clear that these modifications in the electronic spectra induced by precise microstructural features must be taken into account when analysing the transport properties of more realistic magnetic nanostructures.

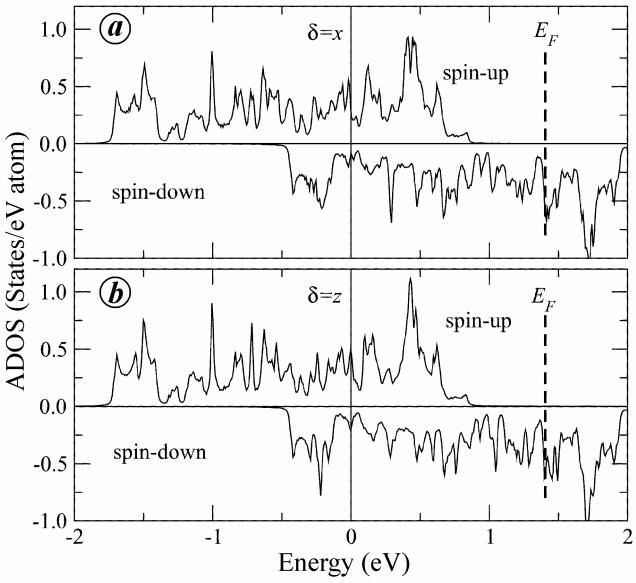

Figure 19. Calculated average density of states (ADOS) for the Co_{195} nanowire shown in Figure 13 *a*. ***a***, The spin-up and spin-down bands for the direction of magnetization $\delta = x$; ***b***, Similar results but for $\delta = z$. The value of the Fermi energy is marked with a vertical dashed line.

Summary and conclusions

In this section, we have reported extensive self-consistent electronic structure calculations dedicated to analyse the MAE as well as the local spin $S_\delta(i)$ and orbital $L_\delta(i)$ magnetic moments for various types of finite length Co nanowires. We have considered monoatomic chains as well as fcc single crystal and polycrystalline nanowires and our calculations have revealed that the local atomic environment has a strong influence on the determination of the easy axis in the structures. We have found strong oscillations of the low energy orientation of the magnetization between parallel and perpendicular directions as the length of the wire increases, or when the geometrical details of the wire-ends are modified. As a general trend, in the polycrystalline atomic configurations we obtain reduced energy differences between parallel and perpendicular directions of magnetization, which could imply that reducing the degree of polycrystallinity in these kind of samples could be used to synthesized magnetic nanowires with a more stable low energy magnetization direction. In addition, it is clear that due to their sensitivity to the local atomic environment, the magnetic properties of these kind of materials can be thus greatly modulated, exploring a wide spectrum of magnetic phenomena.

Finally, we have found a clear dependence of the electronic spectra on the magnetization direction. We have obtained sizable energy shifts and SO-coupling-induced removal of degeneracies all along the energy range, particularly in the case of the polycrystalline configurations, which implies that precise details of the microstructure (i.e. defects, grain boundaries, etc.) in magnetic nanowires

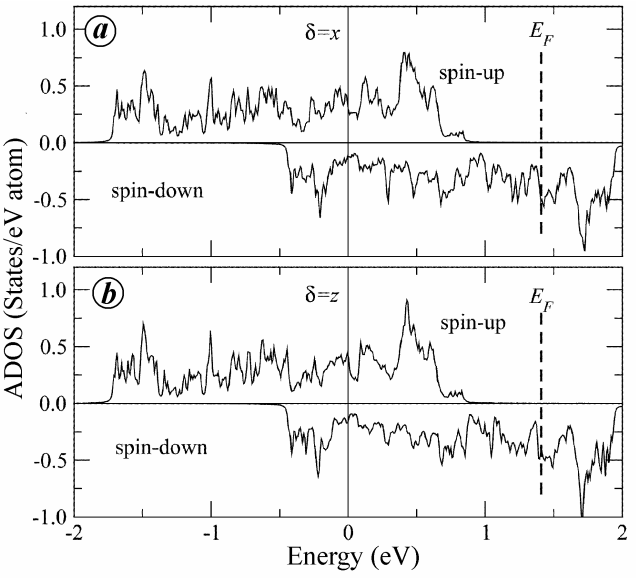

Figure 20. Same as in Figure 19 but for the Co_{183} nanowire shown in Figure 13 *b*.

are expected to strongly modify the number of conduction channels as well as the transport properties of the wires.

Two-dimensional Heusler alloys

The Heusler alloys, are ternary systems X_2MnZ that have been known since 1903 (ref. 73). These systems have manganese as one of the main components and show a rich variety of magnetic phases, depending on the two other chemical components and on the temperature[74,75] that rules the chemical and magnetic order. These alloys looked very promising for applications since the manganese atom has a magnetic moment close to 4 μ_B. These ternary systems crystallize with $L2_1$ structure, and in general the X element is a noble or transition metal and the Z sites are occupied by atoms with *s* and *p* valence electrons. According to a previous calculation[76], the role of the X atoms is to determine the lattice constant and the Z atoms mediate the interactions between Mn atoms. Recently, these alloys have been used for important applications as magnetic shape memory materials[77,78].

The more complex Heusler alloys are those in which the X element is also magnetic. Recently these kind of systems have been intensively studied owing to their great potential for spintronics[79,80], and magnetically driven actuators[81]. One of such systems is Ni_2MnGe. In these systems the magnetic properties of Ni make the alloy more complex but at the same time richer in magnetoelectronic behaviour. Recently these systems have been grown as thin films over a GaAs substrate. The key element for applications in spintronics is the capability to inject electrically spin-polarized carriers into unpolarized semiconductors. It has been found that the bulk Co_2MnSi or Co_2MnGe (ref. 82) alloys there is a gap in the minority sub-band and therefore the up-electrons are the ones free to move.

This study has a two-fold motivation. On one hand, nowadays ultrathin films can be grown with sophisticated techniques which allow depositing multiple chemical elements. For example, recently, by means of thin film-composition spreads, the phase diagram of the Ni–Mn–Ga systems has been studied[83] around the Heusler composition Ni_2MnGa. This alloy is a well known ferromagnetic shape memory alloy. Although the reported results are for relatively thick films, in the range between 500 Å and 1 μm, thinner films, with a two-dimensional character, may be possible to grow. A thin film Heusler alloy may present new properties, characteristic of low dimensional systems. Other point of interest is the possibility to grow half-metallic thin films for spintronic uses.

On the theoretical side, due to the complexity of the three-dimensional Heusler alloys, studies on the interplay of magnetism and chemical order are still lacking[85]. The simplification from three to a two-dimensional system, allows us to study further the chemical and magnetic-order interplay, which rules the properties of these systems. In this part we consider an alloy with Mn as the only magnetic constituent.

Model and calculation

Here, we present the calculation of the ground states of a two dimensional version of a Heusler alloys within a phenomenological model in which only pair-wise interactions, chemical and magnetic are included[85]. The chemical interactions between nearest neighbours of type *I* and *J* are denoted by $V_{I,J}$. The magnetic interaction between the *n*th neighbour manganese atoms are denoted by J_n. In Figure 21 *a*, we show the two-dimensional Heusler lattice model considered here. It is a square lattice in which the four interpenetrating lattices are also square; two of them are occupied by the X atoms, and the other two by the Mn and the Z components. It is interesting to note that our model mimics the two adjacent planes in the (100) direction of the bulk alloy. The X atoms lie in a plane and the other two components, Mn and Z, are located in the interpenetrating lattice of the adjacent plane.

As it has been shown in previous papers[74,75], there are alloys in which, in a wide range of temperatures, the X element does not interchange sites with the other components (Pd_2MnIn, Pd_2MnSn). Thus, one can ignore the two sublattices occupied by the X element and decimate this set of sites. By applying this procedure, we obtain the lattice shown in Figure 21 *b*, where we show only the two square interpenetrating lattices occupied by the elements Mn and Z.

In terms of the chemical and magnetic interactions, the total internal energy of the system can be written like the sum of two contributions

$$E = -\sum_{I,J} N_{I,J} V_{I,J} - \sum_{n}^{3} \sum_{i,j} (\sigma_i \sigma_j)_n J_n, \tag{10}$$

where *I* and *J* denote the Mn and Z atoms, σ_i and σ_j are the magnetic spins of Mn with orientation up (↑) or down (↓), and $n = 1, 2, 3$. For an alloy with a concentration *c* of manganese atoms, Mn_cZ_{1-c}, one can rewrite the equation in the form

$$E = -\frac{1}{2} V_1 N_{\mathrm{MnZ}} + E_c - \sum_{n}^{3} \sum_{i,j} (\sigma_i \sigma_j)_n J_n, \tag{11}$$

where $V_1 = V_{\mathrm{MnMn}} + V_{ZZ} - 2V_{\mathrm{MnZ}}$ is the energy of mixing. At low temperatures, positive values of V_1 drive the alloy to an ordered array while negative ones tend the alloy to separate into two phases. N_{MnZ} is the total number of Mn–Z pairs and E_c is given term of the concentration *c* and the total number of Mn–Mn and Z–Z pairs, i.e. a constant energy of a segregated system. Furthermore, positive

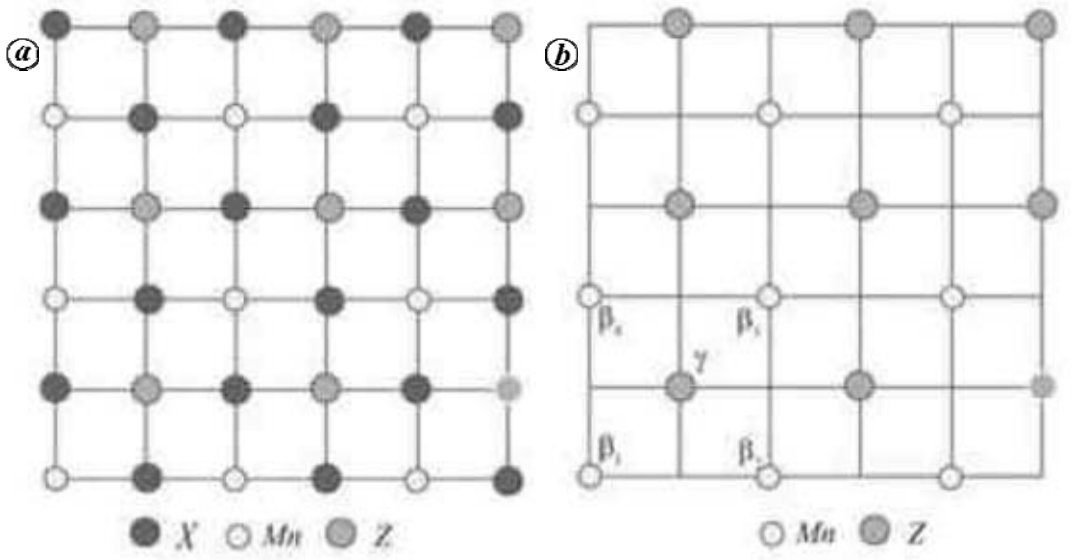

Figure 21. ***a***, The two-dimensional Heusler crystalline structure showing the various sublattices occupied by the *X*, Mn and *Z* elements; ***b***, The decimated lattice containing only the sites occupied by *Y* and *Z* elements.

(negative) values of J_n favour a FM (AF) alignment between the *n*th Mn neighbours. It is important to note that the magnetic interactions between Mn first neighbours favour the formation of Mn pair and contributes to form a segregated alloy. In the case of Heusler alloys, the chemical interactions are much more stronger than the magnetic ones and form ordered patterns at low temperatures.

To calculate the ground states that can be attainable with the interactions considered in our Hamiltonian, we take the five-point cluster shown in Figure 22. We denote the sites of the square vertex β_i, $i = 1, 2, 3, 4$, and the one in the middle by γ. One can notice that in this cell, the number of first, second and third neighbours are $z_1 = 4$, $z_2 = 4$ and $z_3 = 2$ respectively. Since each site can be occupied by Mn↑, Mn↓ or Z, the total number of configurations is $3^5 = 243$, however, many of them are degenerate with a multiplicity λ_r. If we denote the probability to find the *r* configuration by x_r, it follows that

$$\sum_{r=1}^{243} \lambda_r x_r = 1. \tag{12}$$

There is a second constrain that has to be observed and involves the nominal concentration of Mn atoms in the binary system

$$\sum_{r=1}^{243} c_r \lambda_r x_r = c. \tag{13}$$

where c_r is the concentration of Mn atoms in the cluster *r*.

Here, we consider only ordering alloys and by taking into account the symmetry of the cluster one finds that the total number of different configurations reduces to 34. Furthermore, this cluster allows to describe ordered arrangements corresponding to the concentrations $c = 1$, 7/8, 3/4, 5/8, 1/2, 3/8, 1/4, 1/8 and 0. Here we report the case of $c = 1/2$. The characteristics of the configurations that correspond to the equiatomic concentration are given in Table 2. It is important to notice that the configurations with probabilities x_1 and x_5 are equivalent, but the way to construct them is different.

In Figure 22 we present the different possible arrangement within the five-point cluster. All the figures represent a complete ordered alloy with the Mn atoms arranged with different magnetic patterns. There are not Mn atoms as nearest neighbours. In Figure 22 *a* (x_1), the Mn atoms order ferromagnetically (F). In Figure 22 *b* (x_2) the manganese atoms are arranged in alternating diagonals with ferromagnetic and antiferromagnetic coupling (F–AF). A superantiferromagnetic (SAF) pattern is shown in Figure 22 *c* and is represented by x_3. Finally, Figure 22 *d* represents the manganese atoms with AF order denoted by x_4.

Results

Now we proceed to calculate the ground state of the system as a function of the energy parameters. Since *E* is a linear function of the configurational parameters x_i, all possible ordered states are located inside a convex polyhedron in configurational space. The range of stability with respect to the interaction parameters is given by an hypercone with extreme rays defined by the normals to all phases of the configurational polyhedral converging to the vertex in question[87,88].

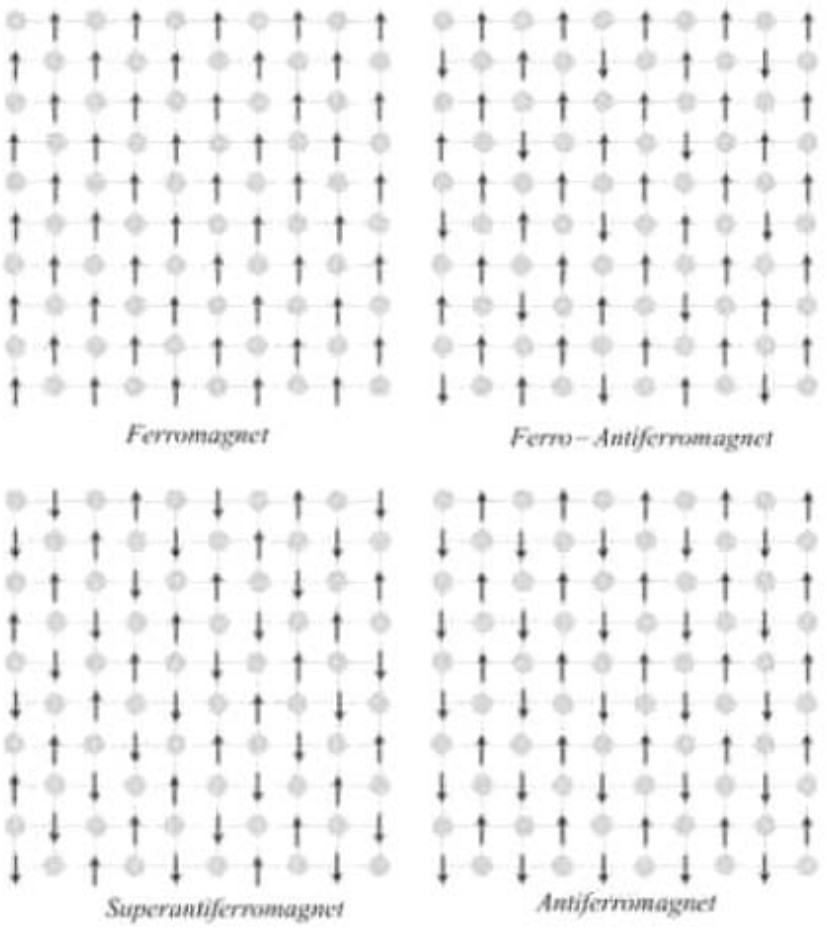

Figure 22. Magnetic phases of the completely ordered Mn–Z alloy: ferromagnetic (F), alternating diagonals with ferromagnetic and antiferromagnetic arrangements (F–AF), superantiferromagnetic (SAF) and antiferromagnetic (AF).

Table 2. Description of the possible configurations x_i, in a five point cluster for the alloy composition $Y_{0.5}Z_{0.5}$. We show the occupation of the various sublattices. Y is the magnetic atom and the magnetic moment can take the directions ↑ and ↓. The open circle denotes the non-magnetic Z element. The symbol λ_r denotes the multiplicity

x_r	β_1	β_2	γ_3	β_3	β_4	λ_r
x_1	↑	↑	○	↑	↑	2
x_2	↓	↑	○	↑	↑	8
x_3	↓	↓	○	↑	↑	4
x_4	↓	↑	○	↓	↑	2
x_5	○	○	↑	○	○	2

The results for the ground states for the system depend on the energy parameters V_{MnZ}, J_2 and J_3, since there are no Mn nearest neighbours. In Figure 23 *a* we show the results in the $V_{12} = V_{MnZ}/J_2$ vs $J_{32} = J_3/J_2$ space and taking negative values for J_2. The only arrangements possible in this part of the space phase are the antiferomagnetic states, SAF and the AF. In the hatched area there are no stable states. The results for a positive coupling J_2 are given in Figure 23 *b*. In this case the accessible states are the ferromagnetic (x_1) and the superantiferromagnetic (x_3) arrangements. Again in the hatched area there are no stable states.

A richer behaviour is obtained when we plot the results in the $V_{13} = V_{MnZ}/J_3$, $J_{23} = J_2/J_3$ (Figure 24). For negative values of J_3 (upper panel) the possible states are ferromagnetic (X_1), the superantiferromagnetic (x_3) and the antiferromagnetic (x_4). We find also a wider area of non-accessible states. For positive values of J_3 (lower panel) the allowed states are the ferromagnetic (x_1) and the antiferromagnetic (x_4) patterns. Bellow the point, *a*, an area of non-accessible states opens.

Finally, we show in Figure 25 the phase diagram in the J_{3V} ($= J_3/V_{MnZ}$) vs J_{2V} ($= J_2/V_{MnZ}$). Figure 26 *a* shows the results for the case $V_{MnZ} < 0$. The possible states are the ferromagnet (x_1), the antiferromagnet (x_4) and the superantiferromagnet (x_3). There is also a part in the centre of the phase diagram in which there are no solutions. The solutions for the case in which $V_{MnZ} > 0$ are presented in the lower panel. The allowed states are the same as in

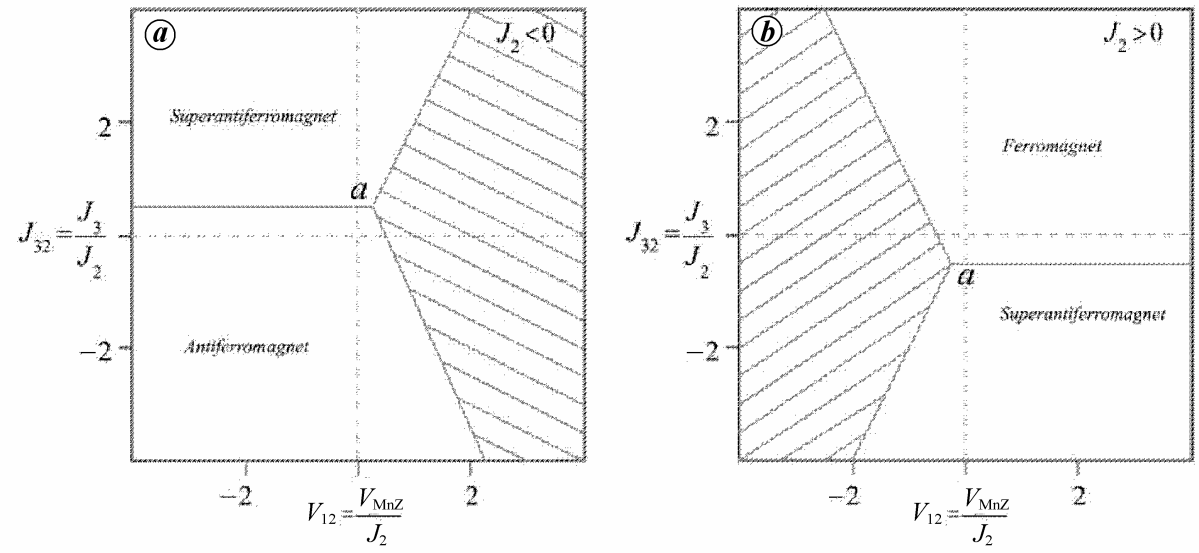

Figure 23. The ground state phase diagram in the V_{12} (= V_{MnZ}/J_2) vs J_{32} (= J_3/J_2) parameter space for systems with $J_2 < 0$ and $J_2 > 0$, upper and lower panels respectively. In the hatched areas there are no ordered solutions.

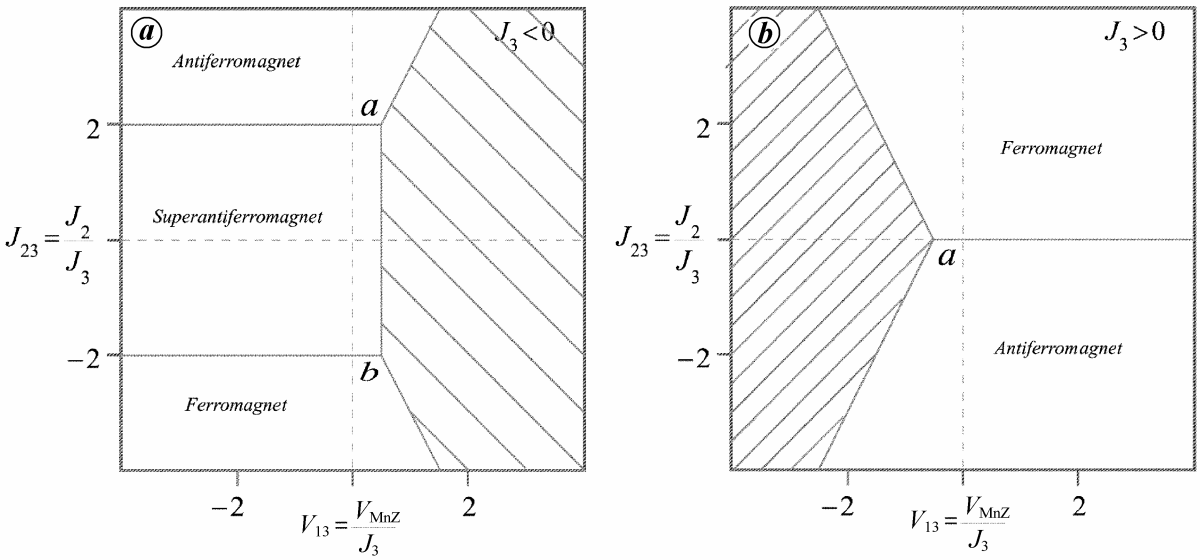

Figure 24. The ground state phase diagram in the V_{13} (= V_{MnZ}/J_3) vs J_{23} (= J_2/J_3) parameter space for systems with $J_3 < 0$ and $J_3 > 0$, upper and lower panels respectively. In the hatched areas there are not ordered alloy solutions.

Figure 26 *a*, but the forbidden area disappears, since $V_{Mn} > 0$ produces an ordered alloy, and there are solutions in all the phase diagram.

Summary

In this section we just touch one of the many Heulser systems. It clearly shows the great potential of these alloys, due to the very rich magnetic behaviour. We presented a simplified version, two dimensional and analysed the magnetic ground states of a Heusler alloy in which the only magnetic component is Mn. This was done in order to reduce the degree of complexity and in an attempt to understand the interplay between chemical order and magnetism.

The possible applications that Heusler alloys have in spintronics and magnetic memory shape devices, make them extremely attractive and many experimental studies are been performed nowadays. We foresee important advances in new technologies based on the magnetic characteristics of these systems.

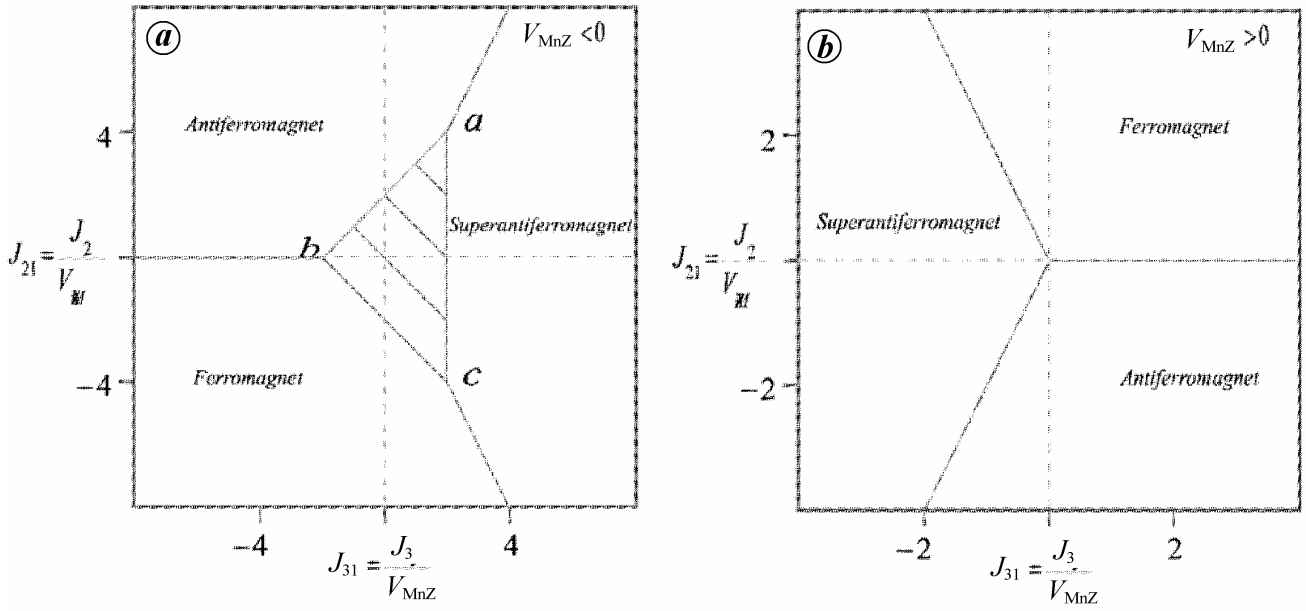

Figure 25. The ground state phase diagram in the J_{3V} ($= J_3/V_{MnZ}$) parameter space for $V_{MnZ} < 0$ and $V_{MnZ} > 0$, upper and lower panels respectively. In the hatched areas there are not ordered alloy solutions.

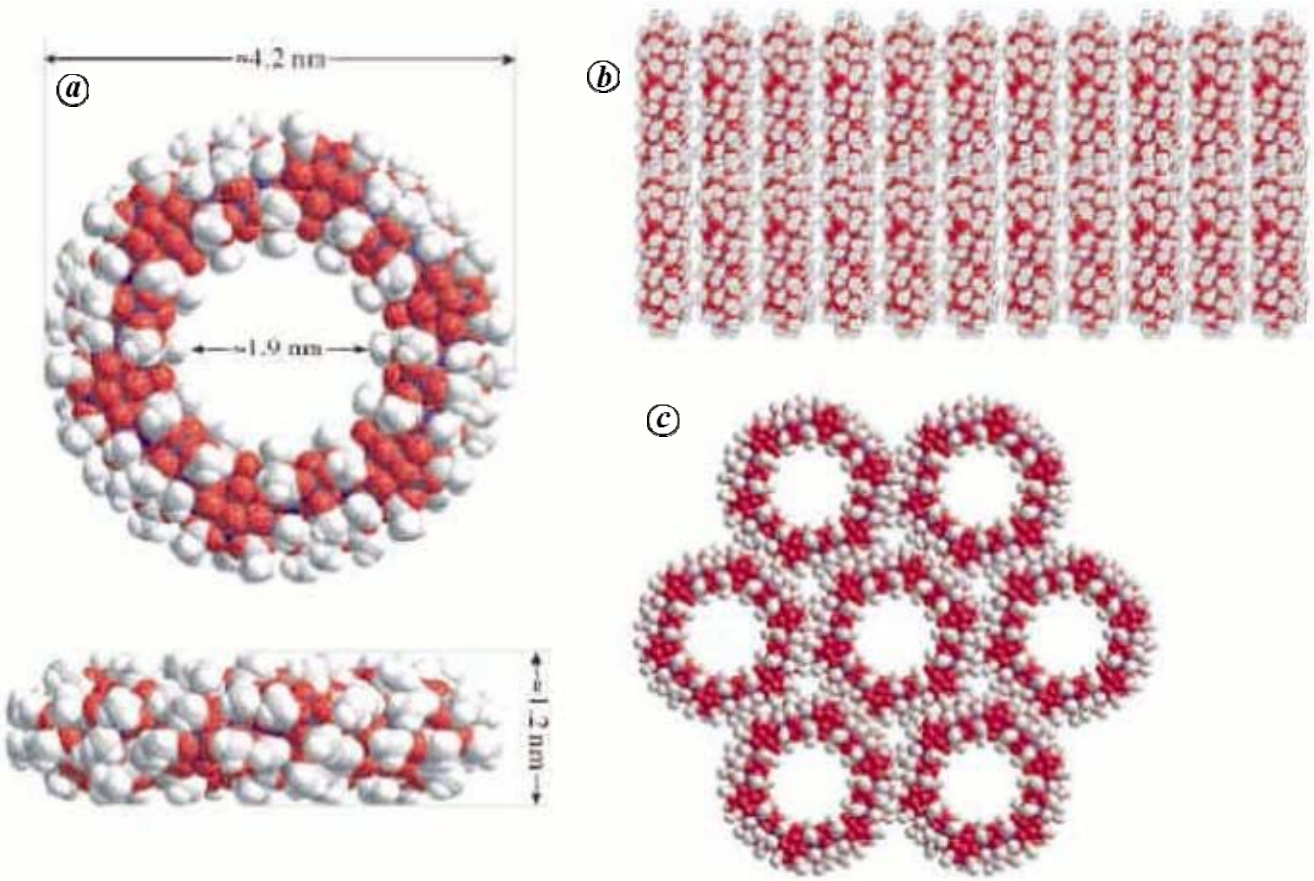

Figure 26. Representations of Mn_{84} and the supramolecular aggregation into ordered nanotubes and sheets. For more detail consult ref. 94. With permission of W. Wernsdorfer.

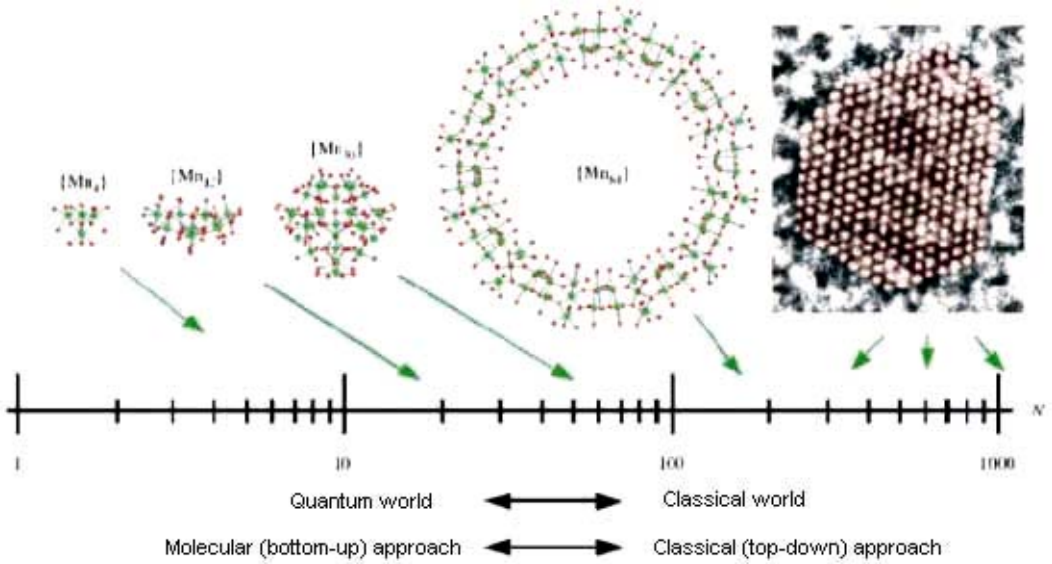

Figure 27. The Neel vector of the Manganese SMMs that have been synthesized, (Mn_4), (Mn_{12}), (Mn_{30}), and (Mn_{84}). For comparison a high-resolution transmission electron microscopy view along a [110] direction of a 3 nm diameter Co nanoparticle containing about 1000 Co atoms[95] is shown. Figure reproduced with the kind permission of W. Wernsdorfer.

Single molecule magnets

The applications of small magnetic systems require monodisperse well-characterized particles. We mentioned before that one possibility is t_0 grow particles or wires in nanoporous membranes by electrodeposition.

Other systems that are naturally monodisperse are what now are called single molecule magnets (SMM). These are intricate molecules with a complex chemical structure with Mn as its main component. They act as single magnetic domains that bellow the blocking temperature show interesting hysteresis loops. The first reported systems[89] contained 12 manganese atoms per unit cell with an effective spin $S = 10$. Thereafter called [Mn_4]. These interesting systems show quantum tunneling of magnetization[90] and quantum phase interference [?]. It is foreseen that quantum tunnelling may be advantageous in applications in quantum computing[91].

More recently other interesting SMM have been synthesized: Mn_{12} (ref. 92), Mn_{30} (ref. 93), and the giant SMM Mn_{84} (ref. 94). All these beautiful molecular solids display magnetic hysteresis and may be suitable for applications. We present in Figure 26 the atomic model for the giant Mn_{84}. It is a torus with diameter of 4.2 nm with a hollow diameter of 1.9 nm. Figure 26 *a* shows views from perpendicular and parallel planes of the torus. The molecules ensemble one on top of the other (Figure 26 *b*) and these units form an hexagonal arrangements (Figure 26 *c*). For details the reader is referred to ref. 94.

In Figure 27 we show (with permission of the author) the Neel vector N for the various SMM. The vector is defined as the sum of the individual spins. $N = 7.5$, 22, 61 and 168 for the four SMM displayed. For comparison a Co nanoparticle is included at the right-hand side. This molecule contains approximately 1000 Co atoms[95].

The study of these supramolecular crystalline, monodisperse systems is a field of current interest and they promise spectacular applications.

General summary

Here we have presented recent studies on the magnetic properties of nanostructured materials. We have gone from the basic unit, a Mn dimer, to huge supramolecules where manganese plays a decisive role. We went from zero to three-dimensional systems through nanowires, and surfaces. The number of systems is enormous but we have restricted to only some particular examples in order to show the richness of the field.

There is no doubt that with the understanding and careful synthesis of these materials, in the near future a new set of miniature gadgets that make use of the magnetic properties of nanostructures will appear in the market.

1. Cox, A. J., Louderback, J. G. and Bloomfield, L. A., Experimental observation of magnetism in rhodium clusters. *Phys. Rev. Lett.*, 1993, **71**, 923–926.
2. Morán-López, J. L., Theoretical studies and modeling of nanostructured materials a challenge for the 1990s. *Computat. Mater. Sci.*, 1994, **2**, 72–80.
3. Isabelle, M. L., Billas, A., Châtelain and Walt A. de Heer, Magnetism from the atom to the bulk in iron, cobalt, and nickel clusters. *Science*, 1994, **265**, 1682–1684.
4. Knickelbein, M. B., Magnetism from the atom to the bulk in iron, cobalt, and nickel clusters. *Phys. Rev. Lett.*, 2001, **86**, 5255–5257.
5. Knickelbein, M. B., Magnetic ordering in manganese clusters. *Phys. Rev.*, **B70**, 2004, 014424.

6. Sorop, T. G., Untiedt, C., Luis, F., de Jongh, L. J., Kröll, M. and Rasa, M., Magnetization reversal of individual Fe nanowires in alumites studied by magnetic force microscopy. *J. Appl. Phys*., 2003, **93**, 7044–7046; Meier, J., Doudin, B. and Ansermet, J.-Ph., Magnetic properties of nanosized wires. *J. Appl. Phys*., 1996, **79**, 6010–6012; Huang, Y. H., Okumura, H. and Hadjipanayis, G. C., CoPt and FePt nanowires by electrodeposition. *J. Appl. Phys*., 2002, **91**, 6869–6871; Fodor, P. S., Tsoi, G. M. and Wenger, L. E., Fabrication and characterization of $Co_{1-x}Fe_x$ alloy nanowires. *J. Appl. Phys*., 2002, **91**, 8186–8188; Zhang, X. Y., Wen, G. H., Chan, Y. F., Zheng, R. K., Zhang, X. X. and Wang, N., Fabrication and magnetic properties of ultrathin Fe nanowire arrays. *Appl. Phys. Lett.*, 2003, **83**, 3341–3343; Snoeck, E., Dunin-Borkowsky, R. E., Dumestre, F., Renaud, P., Amiens, C., Chaudret, B. and Zurcher, P., Quantitative magnetization measurements on nanometer ferromagnetic cobalt wires using electron holography. *Appl. Phys. Lett.*, 2003, **82**, 88–90; Shi, J. B., Chen, Y. J., Lin, Y. T., Wu, C., Chen, C. J. and Lin, J. Y., Synthesis and characteristics of Fe nanowires. *Japan J. Appl. Phys*., 2006, **45**, 9075–9077.
7. Ounadjela, K., Ferré, R., Louail, L., George, J. M., Maurice, J. L. Piraux, L. and Dubois, S., Magnetization reversal in cobalt and nickel electrodeposited nanowires. *J. Appl. Phys.*, 1997, **81**, 5455–5457.
8. Bantu, A. K. M., Rivas, J., Zaragoza, G., López-Quintela, M. A. and Blanco, M. C., Structures and magnetic properties of electrodeposited cobalt nanowires. *J. Appl. Phys.*, 2001, **89**, 3393–3397.
9. Strijkers, G. J., Dalderop, J. H. J., Broeksteeg, M. A. A., Swagten, H. J. M. and de Jonge, W. J. M., Structure and magnetization of arrays of electrodeposited Co wires in anodic alumina. *J. Appl. Phys.*, 1999, **86**, 5141–5145.
10. Pierce, J. P., Plummer, E. W. and Shen, J., Ferromagnetism in cobalt-iron alloy nonowire arrays on W(110). *Appl. Phys. Lett*., 2002, **81**, 1890–1892; Sun, L., Searson, P. C. and Chien, C. L., Finite-size effects in nickel nanowire arrays. *Phys. Rev.*, 2000, **B61**, R6463–R6466.
11. Pignard, S., Goglio, G., Radulescu, A., Piraux, L., Dubois, S., Declémy, A. and Duvail, J. L., Study of the magnetization reversal in individual nickel nanowires. *J. Appl. Phys.*, 2000, **87**, 824–829.
12. Gao, J.-H., Sun, D.-L., Zhan, Q.-F., He, W. and Cheng, Z.-H., Magnetization reversal process and magnetic relaxation of self-assembled Fe_3Pt nanowire arrays with different diameters: experiment and micromagnetic simulations. *Phys. Rev.*, 2007, **B75**, 064421.
13. Mejía-López, J., Romero, A., Garcia, M. E. and Morán-López, J. L., Understanding the elusive magnetic behaviour of manganese clusters. *Phys. Rev*., 2008, **B78**, 134405.
14. Mejía-López, J., Romero, A., Garcia, M. E. and Morán-López, J. L., Noncollinear magnetismo, spin frustation, and magnetic nanodomains in small Mn Clusters. *Phys. Rev.*, 2006, **B74**, 140405.
15. Guirado-López, R. A., Montejano-Carrizales, J. M. and Morán-López, J. L., Spin-reorientation transitions in cobalt nanowires: Role of the micriostructure and finite-size effects. *Phys. Rev*., 2008, **B77**, 134431.
16. Rodríguez-Alba, R., Aguilera-Granja, F. and Morán-López, J. L., submitted to *Solid State Commun*. (in press).
17. Friedman, J. R., Sarachik, M. P., Tejada, J. and Ziolo, R., Macroscopic measurement of resonant magnetization tunneling in high-spin molecules. *Phys. Rev. Lett*., 1996, **76**, 3830–3833.
18. Wensdorfer, W., ALiaga-Alcalde, N., Hendrickson, D. N. and Christou, G., Exchange-biased quantum tunneling in a supramolecular dimmer of single-molecule magnets. *Nature*, 2002, **416**, 406–409.
19. Sessoli, R., Gatteschi, D., Caneshi, A. and Novak, M. A., Magnetic bistability in a metal–ion cluster. *Nature*, 1993, **365**, 141–143.
20. Chu, D., Kenning, G. G. and Orbach, R., Dynamic measurements in a Heisenberg spin glass: CuMn. *Phys. Rev. Lett*., 1994, **72**, 3270–3273.
21. Elbio Dagotto, in *The Physics of Manganites and Related Compounds*, Springer Series in Solid-State Sciences, 2003, vol. 136.
22. Mertes, K. M. *et al.*, Mn_{12}-acetate: a prototypical single molecule magnet. *Solid. State Commun.*, 2003, **127**, 131–139.
23. Baumann, C. A., Van Zee, R. J., Bhat, S. V. and Weltner Jr, W., ESR of Mn_2 and Mn_5 molecules in rare-gas matrices. *J. Chem. Phys*., 1983, **78**, 190–199.
24. Lombardi, J. R. and Davids, B., Periodic properties of force constants of small transition-metal and lanthanide clusters. *Chem. Rev*., 2002, **102**, 2431–2460.
25. Hobbs, D., Hafner, J. and Spišák, D., Understanding the complex metallic element Mn. I. Crystalline and noncollinear magnetic structures of α-Mn. *Phys. Rev.*, 2003, **B68**, 014407.
26. Hafner, J. and Hobbs D. II, Geometric frustration in understanding the complex metallic element Mn. β-Mn, phase stability, and phase transitions. *Phys. Rev*., 2003, **B68**, 014408.
27. Fujihisa, H. and Takemura, K., Stability and the equation of state of α-manganese under ultrahigh pressure. *Phys. Rev*. 1995, **52**, 13257–13260.
28. Bier, K. D., Haslett, T. L., Kirkwood, A. D. and Moskovits, M., The resonance Raman and visible absorbance spectra of matrix isolated Mn_2 and Mn_3. *J. Chem. Phys*., 1988, **89**, 6–12.
29. Nesbet, R. K., Heisenberg exchange interaction of two Mn atoms. *Phys. Rev*., 1964, **135**, A460–A465.
30. Pederson, M. R., Reuse, F. and Khanna, S. N., Magnetic transition in Mn_n (n = 2–8) clusters. *Phys. Rev.*, 1998, **B58**, 5632–5636.
31. Bobadova-Parvanova, P., Jackson, K. A., Srinivas, S. and Horoi, M., Emergence of antiferromagnetic ordering in Mn clusters. *Phys. Rev.*, 2003, **A67**, 061202; Structure, bonding, and magnetism in manganese clusters. *J. Chem. Phys*., 2005, **122**, 014310.
32. Harris, J. and Jones, R. O., Density functional theory and molecular bonding. III. Iron-series dimmers. *J. Chem. Phys*., 1979, **70**, 830–841.
33. Morisato, T., Khanna, S. N. and Kawazoe, Y., First-principles study of the onset of noncollinearity in Mn_n clusters: magnetic arrangements in Mn_5 and Mn_6. *Phys. Rev*., 2005, **B72**, 014435.
34. Bauschlicher Jr, C. W., On the bonding in Mn^{2+}. *Chem. Phys. Lett.*, 1989, **156**, 95–99.
35. Wang, B. and Chen, Z., Magnetic coupling interaction under different spin multiples in neutral manganese dimmer: CASPT2 theoretical investigation. *Chem. Phys. Lett*., 2004, **387**, 395–399.
36. Yamamoto, S., Tatewaki, H., Moriyama, H. and Nakano, H., A study of the ground state of manganese dimer using quasidegenerate perturbation theory. *J. Chem. Phys.*, 2006, **124**, 124302.
37. Artacho, E., Sánchez-Portal, D., Ordejón, P., García, A. and Soler, J. M., Linear-scaling *ab initio* calculations for large and complex systems. *Phys. Status Solidi*, 1999, **B215**, 809–817.
38. Oda, T., Pasquarello, A. and Car, R., Fully unconstrained approach to noncollinear magnetism: application to small Fe clusters. *Phys. Rev. Lett.*, 1998, **80**, 3622–3625.
39. Troullier, N. and Martins, J. L., Efficient pseudopotentials for plane-wave calculations. *Phys. Rev.*, 1991, **B43**, 1993–2006.
40. Van Zee, R. J., Baumann, C. A., Bhat, S. V. and Weltner Jr, W., ESR of the high-spin (S = 25/2) Mn_5 molecule. *J. Chem. Phys*., 1982, **76**, 5636–5637.
41. Briere, T. M., Sluiter, M. H. F., Kumar, V. and Kawazoe, Y., Atomic structures and magnetic behaviour of Mn clusters. *Phys. Rev*., 2002, **B66**, 064412.
42. Ferre, R., Ounadjela, K., George, J. M., Piraux, L. and Dubois, S., Magnetization processes in nickel and cobalt electrodeposited nanowires. *Phys. Rev.*, 1997, **B56**, 14066–14075.
43. García, J. M., Asenjo, A., Velázquez, J., García, D. and Vázquez, M., Magnetic behaviour o fan array of cobalt nanowires. *J. Appl. Phys*., 1999, **85**, 5480–5482.

44. Lu, X., Ge, S., Jiang, L. and Wang, X., Chain of ellipsoids approach to the magnetic nanowire. *J. Appl. Phys*., 2005, **97**, 084304.
45. Fodor, P. S., Tsoi, G. M. and Wenger, L. E., Modeling of hysteresis and magnetization curves for hexagonally ordered electrodeposited nanowires. *J. Appl. Phys.*, 2003, **93**, 7438–7440.
46. Krüuger, B., Pfannkuche, D., Bolte, M., Meier, G. and Merkt, U., Current-driven domain-wall dynamics in curved ferromagnetic nanowires. *Phys. Rev.*, 2007, **B75**, 054421.
47. Lazarovitz, B., Szunyogh, L., Weinberger, P. and Újfalussy, B., Magnetic properties of finite Fe chains at fcc Cu(001) and Cu(111) surfaces. *Phys. Rev.*, 2003, **B68**, 024433.
48. Klautau, A. B. and Frota-Pessoa, S., Magnetic properties of Co nanowires on Cu(001) surfaces. *Phys. Rev.*, 2004, **70**, 193407.
49. Komelj, M., Ederer, C., Davenport, J. W. and Fähnle, M., From the bulk to monatomic wires: An *ab initio* study of magnetism in Co systems with various dimensionality. *Phys. Rev*., 2002, **B66**, 140407.
50. Hong, J. and Wu, R. Q., First principles calculations of magnetic anisotropy energy of Co monatomic wires. *Phys. Rev.*, 2003, **B67**, 020406.
51. Dorantes-Dávila, J. and Pastor, G. M., Magnetic anisotropy of one-dimensional nanostructures of transition metals. *Phys. Rev. Lett*., 1998, **81**, 208–211.
52. Gambardella, P. *et al.*, Growth of composition-modulated Ag/Co wires on Pt(997). *Phys. Rev.*, 2001, **B64**, 045404.
53. Druzinić and Hübner, W., Nonperturbative theory of magnetocrystalline anisotropy energyfor wires and rings of Fe adatoms. *Phys. Rev*., 1997, **B55**, 347–355.
54. Mokrousov, Y., Bihlmayer, G., Heinze, S. and Blügel, S., Giant magnetocrystalline anisotropies of 4*d* transition–metal monowires. *Phys. Rev. Lett*., 2006, **96**, 147201.
55. Desjonqueres, M. C., Barreteau, C., Autes, G. and Spanjaard, D., Orbital contribution to the magnetic properties of iron as a function of dimensionality. *Phys. Rev*., 2007, **B76**, 024412.
56. Viret, M., Gabureac, M., Ott, F., Fermon, C., Barreteau, C., Autes, G. and Guirado-López, R., Giant anisotropic magneto-resistance in ferromagnetic atomic contacts. *Eur. Phys. J*., 2006, **B51**, 1–4.
57. Fujita, T., Hayashi, Y., Tokunaga, T. and Yamamoto, K., Cobalt nanorods fully encapsulated in carbon nanotube and magnetization measurements by off-axis electron holography. *Appl. Phys. Lett*., 2006, **88**, 243118.
58. Pastor, G. M., Dorantes-Davila, J., Pick, S. and Dreyssé, H., Magnetic anisotropy of 3*d* transition-metal clusters. *Phys. Rev. Lett*., 1995, **75**, 326–329.
59. Rodríguez-López, J. L., Dorantes-Dávila, J. and Pastor, G. M., Orbital magnetism at the surfaces of 3d transition metals. *Phys. Rev.*, 1998, **B57**, 1040–1045.
60. Félix-Medina, R., Dorantes-Dávila, J. and Pastor, G. M., Ground-state magnetic properties of Co_N clusters on Pd(111): spin moments, orbital moments, and magnetic anisotropy. *Phys. Rev.*, 2003, **B67**, 094430.
61. Friedel, J., Lenglart, P. and Leman, G., Etude du couplage spin-orbite dans les metaux de transition. Application au platine. *J. Phys. Chem. Solids*, 1964, **25**, 781–800.
62. Bruno, P., *Magnetismus von Festkörpern und Grenzflächen, Ferienkurse des Forschungszentrums Jülich* (KFA Jülich, 1993), ISBN 3-89336-110-3, Ch. 24.
63. Haydock, R., In *Solid State Physics* (eds Ehrenreich, H., Seitz, F. and Turnbull, D.), Academic, New York, 1980, vol. 35, p. 215.
64. Heine, V., S–D interaction in transition metals. *Phys. Rev.*, 1967, **153**, 673–682.
65. Moruzzi, V. L. and Marcus, P. M., In *Handbook of Magnetic Materials* (eds Buschow, K. H. J.), Elsevier, 1993, vol. 7.
66. Guirado-López, R., Magnetic anisotropy of fcc transition-metal clusters: role of surface relaxation. *Phys. Rev.*, 2001, **B63**, 174420.
67. Guirado-López, R. and Montejano-Carrizales, J. M., Orbital magnetism and magnetic anisotropy energy of Co nanoparticles: role of polytetrahedral packing, polycrystallinity, and internal defects. *Phys. Rev.*, 2007, **B75**, 184435.
68. Dorantes-Dávila, J., Dreyssé, H. and Pastor, G. M., Exchange interaction and local environment effects on the magnetic properties of Fe_N clusters. *Phys. Rev.*, 1992, **B46**, 10432–10436; Piveteau, B., Desjonquères, M. C., Olés, A. M. and Spanjaard, D., Magnetic properties of 4*d* transition-metal clusters. *Phys. Rev.*, 1996, 9251–9266.
69. Dorantes-Dávila, J., Dreyssé, H. and Pastor, G. M., Magnetic anisotropy of close-packed (111) ultrathin transition-metal films: role of interlayer packing. *Phys. Rev.*, 1997, **55**, 15033–15042.
70. Wende, H., Scherz, A., Wihelm, F. and Baberschke, K., Induced magnetism at thin-film interfaces probed by means of X-ray magnetic circular dichroism. *J. Phys.: Condens. Matter*, 2003, **15**, S547–S559.
71. Yang, J. B., Xu, H., You, S. X., Zhou, X. D., Wang, C. S., Yelon, W. B. and James, W. J., Large scale growth and magnetic properties of Fe and Fe_3O_4 nanowires. *J. Appl. Phys*., 2006, **99**, 08Q507.
72. Lessard, A., Moss, T. H. and Hübner, W., Magnetocrystalline anisotropy energy of transition-metal thin films: A nonperturbative theory. *Phys. Rev.*, 1997, **B56**, 2594–2604.
73. Heusler, F., Verh. Dtsch. *Phys. Ges*., 1903, **5**, 219.
74. Webster, P. J. and Tabble, R. S., Magnetic and chemical order in Pd_2MnAl in relation to order in the Heusler alloys Pd_2MnIn, Pd_2MnSn, and Pd_2MnSb. *J. Appl. Phys*., 1968, **39**, 471–473.
75. Webster, P. J. and Ramadan, M. I., Magnetic order in palladium-based Heusler alloys Part I: $Pd_2MnIn_{1-x}Sn_x$ and $Pd_2MnSn_{1-x}Sb_x$. *J. Mag. Mag. Mater*., 1977, **5**, 51–59.
76. Kubler, J., Williams, A. R. and Sommers, C. R., Formation and coupling of magnetic moments in Heusler alloys. *Phys. Rev.*, 1983, **B28**, 1745–1755.
77. Vasilev, A. N., Klestov, S. A., Levitin, R. Z., Snegirev, V. V., Kokorin, V. V. and Chernenko, V. A., *J. Exp. Theor. Phys*., 1996, **82**, 524.
78. Zhang, M., Bruck, E., de Boer, F. R. and Wu, G., Magnetic, martensitic transformation, magnetostriction and shape memory effect in $Co_{50}Ni_{20}Ga_{30}$ melt-spun ribbons. *J. Phys.*, 2005, **D38**, 1361–1364.
79. Galanskis, I., Dederich, P. H. and Papanikolaou, N., Origin and properties of the gap in the half-ferromagnetic Heusler alloys. *Phys. Rev*., 2002, **B66**, 134428.
80. Orgassa, D., Fusiwara, H., Schulthess, T. C. and Buttler, W. H., First-principles calculation of the effect of atomic disorder on the electronic structure of the half-metallic ferromagnet NiMnSb. *Phys. Rev.*, 1999, **B60**, 13237–13240.
81. Ullakko, K., Huang, J. K., Kantner, C., Ohandly, R. C. and Kokorin, V. V., Large magnetic-field-induced strains in Ni_2MnGa single crystals. *Appl. Phys. Lett*., 1966, **69**, 1966–1968.
82. Picozzi, S., First-principles study if ferromagnetic Heusler alloys: An overview. In *Advances in Solid State Physics*, 2008, vol. 47, pp. 129–141.
83. Takeuchi, I. *et al.*, Identification of novel compositions of ferromagnetic shape-memory alloys using composition spreads. *Nature Mater*., 2003, **2**, 180–184.
84. Ishida, Y., *Physica*, 1977, **B91**, 130.
85. Moran-Lopez, J. L., Rodriguez-Alba, R. and Agulera-Granja, F., Modeling the magnetic properties of Heusler alloys. *J. Mag. Mag. Mater*., 1994, **131**, 417–426.
86. Zayak, A. T., Entel, P., Rabe, K. M., Adeagbo, W. A. and Acet, M., Anomalous vibrational effects in nonmagnetic and magnetic Heusler alloys. *Phys. Rev*., 2005, **B72**, 054113.
87. Allen, S. M. and Cahn, J. W., Coherent and incoherent equilibria in iron–rich iron–aluminum alloys. *Acta Metall.*, 1975, **23**, 1017–1026.
88. Sanchez, J. M. and de Fontaine, D., In *Structure and Bonding in Crystals* (eds Keeffe, M. O. and Navrotsky, A.), Academic, New York, 1981, vol. II, p. 117.

89. Sessoli, R., Gatteschi, D., Caneschi, A. and Novak, M. A., *Nature*, 1993, **365**, 141.
90. Friedman, J. R., Sarachik, M. P., Tejada, J. and Ziolo, R., Macroscopic measurement of resonant magnetization tunneling in high-spin molecules. *Phys. Rev. Lett.*, 1996, **76**, 3830–3833.
91. Leuenberger, N. H. and Loss, D., Quantum computing in molecular magnets. *Nature*, 2001, **410**, 789–793.
92. Thomas, L., Lionti, F., Ballou, R., Gateschi, D., Sessoli, R. and Barbara, B., Macroscopic quantum tunnelling of magnetization in a single crystal of nanomagnets. *Nature*, 1996, **386,** 145–147.
93. Soler, M., Rumberger, E., Folting, K., Hendrickson, D. N. and Christou, G., Synthesis, characterization and magnetic properties of $[Mn_{30}O_{24}(OH)_8(O_2CCH_2C(CH_3)_3)_{32}(H_2O)_2(CH_3NO_2)_4]$: the largest manganese carboxylate cluster. *Polyhedron*, 2001, **20**, 1365–1369.
94. Tasiopolus, A. J., Vinslava, A., Wernsdorfer, W., Abboud, K. A. and Christou, G., Giant single-molecule magnets: a {Mn84} torus and its supramolecular nanotubes. *Angew. Chem. Int. Ed.*, 2004, **43**, 2117.
95. Jamet, M., Wernsdorfer, W., Thirion, C., Mailly, D., Dupuis, V. P. Melinon, V. and Perez, A., Macroscopic quantum tunneling of magnetization of single ferrimagnetic nanoparticles of barium ferrite. *Phys. Rev. Lett.*, 1997, **79**, 4014–4017.

ACKNOWLEDGEMENTS. J.L.M.-L. acknowledges the support of the J. Tinsley Oden Faculty Fellowship Research Program in the Institute for Computational Engineering and Sciences at the University of Texas at Austin. J.M. acknowledges support FONDECYT under grants 1050066 and 7050111, and from the Millennium Sciences Nucleus 'Condensed Matter Physics' P02-054F. M.E.G. acknowledges the kind hospitality at the IPICYT and also support from the DFG through the grant SPP1153. A.H.R., R.A.G.-L., J.M.M.-C and J.L.M.-L. would like to acknowledge the financial support from CONACyT through grants J-42647-F, 45928-F, 50650 and 61417 respectively. Computer resources from the Centro Nacional de Supercumputo (CNS) from the Instituto Potosino de Investigacion Cienti_ca y Tecnologica (IPICyT). San Luis Potosi, Mexico, are also acknowledged.